JMEPEG
DOI: 10.1007/s11665-013-0583-2

1059-9495/$19.00

Multiphysics Modeling and Simulations of Mil A46100 Armor-Grade Martensitic Steel Gas Metal Arc Welding Process

M. Grujicic, S. Ramaswami, J.S. Snipes, C.-F. Yen, B.A. Cheeseman, and J.S. Montgomery

(Submitted January 18, 2013; in revised form April 3, 2013)

A multiphysics computational model has been developed for the conventional Gas Metal Arc Welding (GMAW) joining process and used to analyze butt-welding of MIL A46100, a prototypical high-hardness armor martensitic steel. The model consists of five distinct modules, each covering a specific aspect of the GMAW process, i.e., (a) dynamics of welding-gun behavior; (b) heat transfer from the electric arc and mass transfer from the electrode to the weld; (c) development of thermal and mechanical fields during the GMAW process; (d) the associated evolution and spatial distribution of the material microstructure throughout the weld region; and (e) the final spatial distribution of the as-welded material properties. To make the newly developed GMAW process model applicable to MIL A46100, the basic physical-metallurgy concepts and principles for this material have to be investigated and properly accounted for/modeled. The newly developed GMAW process model enables establishment of the relationship between the GMAW process parameters (e.g., open circuit voltage, welding current, electrode diameter, electrode-tip/weld distance, filler-metal feed speed, and gun travel speed), workpiece material chemistry, and the spatial distribution of as-welded material microstructure and properties. The predictions of the present GMAW model pertaining to the spatial distribution of the material microstructure and properties within the MIL A46100 weld region are found to be consistent with general expectations and prior observations.

Keywords Gas Metal Arc Welding (GMAW), MIL A46100, multiphysics process modeling

1. Introduction

The subject of this study is computational modeling and simulation of the conventional Gas Metal Arc Welding (GMAW) process, and the application of the developed methods and tools for prediction of the microstructure evolution and the local properties within the weld region (consisting of the solidified weld pool, also referred to as the Fusion Zone, FZ, and the adjacent heat-affected zone, HAZ) of a prototypical high-hardness armor-grade martensitic steel MIL A46100 (Ref 1). It is hoped that the availability of such a process model will help in identifying optimal GMAW process parameters which maximize welding process throughput while ensuring the formation of sound/high-quality welds with the minimal welding-induced degradation of weld-region properties (relative to those of the welding-unaffected base-metal). In addition, provided that the model/simulations can be made highly efficient computationally, they can be used for real-time control of the GMAW process. Based on the foregoing, the concepts most pertinent to this study are: (a) the fundamentals of the GMAW process; (b) steel-weldment microstructure evolution during the welding process; and (c) an overview of the prior modeling and simulation efforts dealing with the GMAW process and with the prediction of the welding-induced changes in the material microstructure and properties. These three aspects are reviewed briefly in the remainder of this section.

1.1 The Fundamentals of Gas Metal Arc Welding

1.1.1 Taxonomy. Joining of metal components by welding is an important technology in many industries such as chemical, oil, aerospace, and shipbuilding construction. In fact, within the metal fabrication industry as a whole, the number of jobs within the welding sector is higher than in any other sector except for assembly and machining (Ref 2). There are a number of ways to classify welding processes. According to one of these classifications, all welding processes are divided into the following categories: (a) resistance welding; (b) arc welding; (c) oxyfuel welding; (d) laser welding; (e) friction-based welding; and (f) other welding processes (Ref 3). Arc welding processes are generally classified into consumable and non-consumable electrode processes. The GMAW process, the subject of this study, falls into the category of consumable electrode arc welding processes along with shielded metal arc welding and submerged arc welding.

1.1.2 Process Description. The two defining characteristics of the GMAW process are: (a) the heat required for the filler-metal melting is generated by means of an electrical arc established between a continuously fed filler-metal wire-shape consumable electrode and the workpiece components to be

M. Grujicic, S. Ramaswami, and **J.S. Snipes**, Department of Mechanical Engineering, Clemson University, 241 Engineering Innovation Building, Clemson, SC 29634-0921; and **C.-F. Yen, B.A. Cheeseman,** and **J.S. Montgomery**, Army Research Laboratory – Survivability Materials Branch, Proving Ground, Aberdeen, MD 21005-5069. Contact e-mail: gmica@clemson.edu.

Published online: 23 May 2013

Report Documentation Page

Form Approved
OMB No. 0704-0188

1. REPORT DATE	2. REPORT TYPE	3. DATES COVERED
23 MAY 2013		**00-00-2013 to 00-00-2013**

4. TITLE AND SUBTITLE	5a. CONTRACT NUMBER
Multiphysics Modeling and Simulations of Mil A46100 Armor-Grade Martensitic Steel Gas Metal Arc Welding Process	5b. GRANT NUMBER
	5c. PROGRAM ELEMENT NUMBER
6. AUTHOR(S)	5d. PROJECT NUMBER
	5e. TASK NUMBER
	5f. WORK UNIT NUMBER
7. PERFORMING ORGANIZATION NAME(S) AND ADDRESS(ES) **Clemson University,Department of Mechanical Engineering,241 Engineering Innovation Building,Clemson,SC,29634**	8. PERFORMING ORGANIZATION REPORT NUMBER
9. SPONSORING/MONITORING AGENCY NAME(S) AND ADDRESS(ES)	10. SPONSOR/MONITOR'S ACRONYM(S)
	11. SPONSOR/MONITOR'S REPORT NUMBER(S)

12. DISTRIBUTION/AVAILABILITY STATEMENT
Approved for public release; distribution unlimited

13. SUPPLEMENTARY NOTES

14. ABSTRACT

15. SUBJECT TERMS

16. SECURITY CLASSIFICATION OF:			17. LIMITATION OF ABSTRACT	18. NUMBER OF PAGES	19a. NAME OF RESPONSIBLE PERSON
a. REPORT	b. ABSTRACT	c. THIS PAGE			
unclassified	**unclassified**	**unclassified**	**Same as Report (SAR)**	**20**	

joined; and (b) an externally supplied shielding gas (or mixture of gases) is employed to protect the welding process zone from the oxidizing/contaminating environment (Ref 4). A labeled schematic of the conventional gas metal arc butt (side-to-side) welding process is shown in Fig. 1. In order to maintain a stable electrical arc during this process, the feeding of the filler-metal wire and shielding gas supply are usually automated.

1.1.3 Advantages and Limitations. Since a detailed overview of the key advantages and limitations of the GMAW process was provided in our recent work (Ref 5, 6), a similar overview will not be given here.

1.1.4 Electrode-to-Weld Material Transfer. Since GMAW is one of the consumable electrode arc welding processes, welding is accompanied by transfer of the molten filler-metal into the gap (or weld-pool) between the components to be joined. Depending on the selection of the GMAW process parameters, metal transfer can occur in one of the following five modes (Ref 4): (a) short-circuit mode; (b) globular mode; (c) spray mode; (d) pulsed mode; and (e) high current density mode. Since a detailed overview of these metal-transfer modes was provided in our recent work (Ref 5, 6), a similar overview will not be given here.

1.1.5 Process Parameters. The main GMAW process parameters are as follows (Ref 4): (a) temporal profile and mean value of the welding current/voltage; (b) composition of the filler-metal; (c) electrode length and diameter; (d) filler-wire feed rate; (e) welding-gun travel speed; (f) composition and flow-rate of the shielding gas; (g) workpiece material(s); and (h) geometry, size, and orientation of the weld.

1.2 Steel-Weldment Microstructure Evolution During the Welding Process

1.2.1 FZ and HAZ Thermal Cycles. As described above, GMAW involves the melting and transfer of a filler-metal into the gap/weld pool between the components to be joined. In addition to producing the heat required for the filler-metal melting, the electric arc is also responsible for direct melting of the components' base metal(s) and for the formation of the weld pool/FZ. In addition, the electro-magnetic forces associated with the arc cause stirring of the molten metal within the weld pool, significantly affecting heat transfer within the weld pool and, in turn, temperature distribution and thermal history of the material in the entire weld (i.e., FZ + HAZ) region (Ref 7). As seen in Fig. 1, as the welding-gun advances along the weld line, the previously formed weld pool begins to cool and finally undergoes complete solidification. The resulting solid material within the FZ continues to cool and, consequently, may undergo several (material-system and thermal history dependent) solid-state phase transformations and microstructure evolution/reorganization processes (Ref 8-10). In addition to the FZ, the HAZ also experiences a thermal cycle (characterized by rapid heating to a peak temperature and subsequent slower cooling to room temperature) and the accompanying solid-state phase transformations and microstructure evolution/reorganization processes. However, the HAZ peak temperature (which depends on the distance of the material point in question from the weld centerline) is not high enough to cause base-material melting. Due to the aforementioned microstructural changes experienced by the filler-metal/base-metal mixture within the FZ and the base metal alone within the HAZ, it is generally found that the overall mechanical (e.g., strength, toughness, ductility, etc.) and environmental resistance (e.g., corrosion resistance) properties of the weldments may significantly differ from their counterparts in the base-metal. The extent of these differences is typically highly dependent on the welding-induced local thermal histories of the material within the FZ and the HAZ, as well as by the choice of the filler-metal.

1.2.2 Microstructural Changes Within Steel-Based Welds. The nature of the phases and the type of microstructure present in the base-metal, as well as in the weld region, are the function of the base-metal chemical composition (as well as of the associated thermomechanical treatment). The subject of this study is a prototypical armor grade high-hardness martensitic steel (MIL A46100). Consequently, when analyzing microstructural and property changes within the FZ and HAZ, attention is focused here on steels in general and on MIL A46100 in particular. In general, material within the FZ and HAZ may undergo a number of phase transformations, both during heating and during subsequent cooling. Nevertheless, if details regarding the displacive/diffusionless (e.g., bainitic, martensitic) phase transformations and the diffusional phase-transformations which produce microstructural constituents (e.g., pearlite) from austenite, as well as alloy-carbide precipitation reactions, are ignored, then the material within the FZ generally undergoes the following sequence of phase transformations: liquid $\rightarrow$ δ-ferrite $\rightarrow$ γ-austenite $\rightarrow$ α-ferrite, while material within the HAZ undergoes the following sequence of phase transformations: martensite $\rightarrow$ γ-austenite $\rightarrow$ α-ferrite (Ref 4).

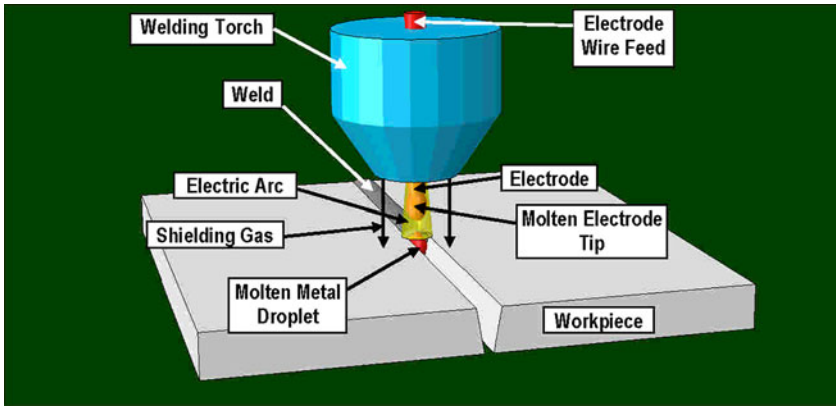

Fig. 1 A schematic representation of the conventional GMAW process

For steel-based welds in general, it has been experimentally (Ref 1) established that: (a) the solidification process and the resulting macro- and micro-structure (including porosity and alloying-element segregation) within the FZ are responsible for the overall soundness of the weld; and (b) the material region within the FZ or HAZ which is associated with the most inferior (thermal-history-governed and material-system-dependent) mechanical properties governs the overall structural (as well as ballistic-protection) performance of the weldment (Ref 11, 12). These observations/findings, along with the concept of microstructure/property relationship, clearly underline the role of the material thermal history within the weld region on the rate and extent of the associated solid-state phase transformations and microstructure evolution/reorganization processes.

1.2.3 Experimental Characterization of the Weld Microstructure. To experimentally characterize the microstructure of GMAW joints, the following three real-time and post-mortem techniques have been generally employed: (a) dilatometry (Ref 13); (b) spatially and time-resolved x-ray diffraction (Ref 7); and (c) post-mortem weld-region material-microstructure microscopy, diffraction, scattering, and spectroscopy-based characterization techniques. Since a detailed overview of these techniques and their main advantages and limitations was provided in our recent work (Ref 5, 6), a similar overview will not be given here.

1.3 Prior GMAW-Process Modeling and Simulation Efforts

As discussed in our recent work (Ref 5, 6), there have been a number of public-domain reports dealing with numerical modeling and simulations of the GMAW process. In general, these modeling and simulation efforts focus only on some aspects of the GMAW process, while the other aspects of this process are either not considered or their treatment is over-simplified. Closer examination of these efforts suggested that they all could be divided into three categories: (a) GMAW models in the first category focus on the dynamics of the electric arc (Ref 14), and on the various aspects of heat and mass transfer from the arc/electrode to the weld pool (Ref 15-23); (b) within the second category of GMAW models, various aspects of the heat and mass flow within the weld pool (Ref 24-27) as well as the heat transfer across the FZ/HAZ boundaries (including the accompanying FZ solidification process) (Ref 28, 29); and (c) within the third category of the GMAW process models, emphasis is placed on predicting microstructure and property evolution within the FZ and HAZ as a function of the base-metal chemistry, initial microstructure of the base-metal, (typically assumed) initial temperature and flow fields in the weld pool, and the thermal history at various locations within the FZ and HAZ (Ref 5-7, 30). As mentioned above, these three categories of GMAW process models neglect the fact that the GAMW is a complex process and that its adequate modeling entails a multiphysics (i.e., multidisciplinary) approach. A first step toward developing a multiphysics GMAW process model is reported here.

1.4 Main Objective

The main objective of this study is to construct a preliminary multiphysics GMAW process model capable of relating the GMAW process parameters, workpiece-material chemistry and microstructure, and weld geometry to the temporal evolution and the spatial distribution of material microstructure within the FZ and HAZ. It should be noted that the aspects of the newly proposed multiphysics GMAW process model dealing with microstructure evolution as a function of the local welding-induced thermal cycle can be considered as an extension of our prior efforts as reported in Ref 5, 6. It should also be noted that, in order to validate the present modeling and simulation approach, some key results obtained are compared with their experimental counterparts, reported in the open literature.

1.5 Organization of the Paper

A detailed description of key aspects of the newly developed multiphysics GMAW process model and its five modules is presented in section 2. In the same section, a brief overview is provided of the basic physical-metallurgy concepts and principles related to MIL A46100 and the associated family of armor-grade high-hardness martensitic steels. The key results pertaining to the effect of GMAW process parameters on the spatial distribution of the principal crystallographic phases and microconstituents, as well as material properties, within the FZ and HAZ of a MIL A46100 GMAW butt weld are presented and discussed in section 3. The main conclusions resulting from this study are summarized in section 4.

2. Multiphysics GMAW Process Model

In this section, details are presented regarding a newly developed multiphysics GMAW process model. The model consists of a sequence of five modules, each focusing on particular aspects of the Friction Stir Welding (FSW) process while ensuring proper connectivity with the adjacent modules. A flowchart-type schematic is shown in Fig. 2 depicting the basic structure of the new multiphysics GMAW process model. More detailed discussions regarding the governing functional relationships, parameterization/calibration, and validation of each of the modules are given in the remainder of this section.

2.1 Welding-Gun Module

Within this module, relationships are established between the welding-gun input parameters: (a) open-circuit voltage; (b) welding current; (c) electrode diameter; (d) electrode-tip/weld distance; (e) filler-metal feed speed; and (f) gun travel speed, and the output parameters, primarily the output heat power and the molten filler-metal deposition rate. In this study, no effort was made to advance significantly the welding-gun modeling efforts beyond the ones already reported in the open literature (Ref 31). It should be noted, however, that the functional relationships mentioned above could also be established using a purely experimental/empirical approach conducted beforehand. Within such an approach, a parametric study over the aforementioned welding-gun input parameters is carried out while the output parameters voltage, current, power, and deposition/spray rate are directly measured. The results obtained are then used either within a multiple regression or a neural network-type procedure to establish and parameterize the welding-gun governing relations.

2.2 Electric-Arc-Based Heat-Source/Metal Spray Module

Within this module, the output heat power and the molten filler-metal deposition rate, as generated in the first module, are used to compute the distribution of the heat-flux and the

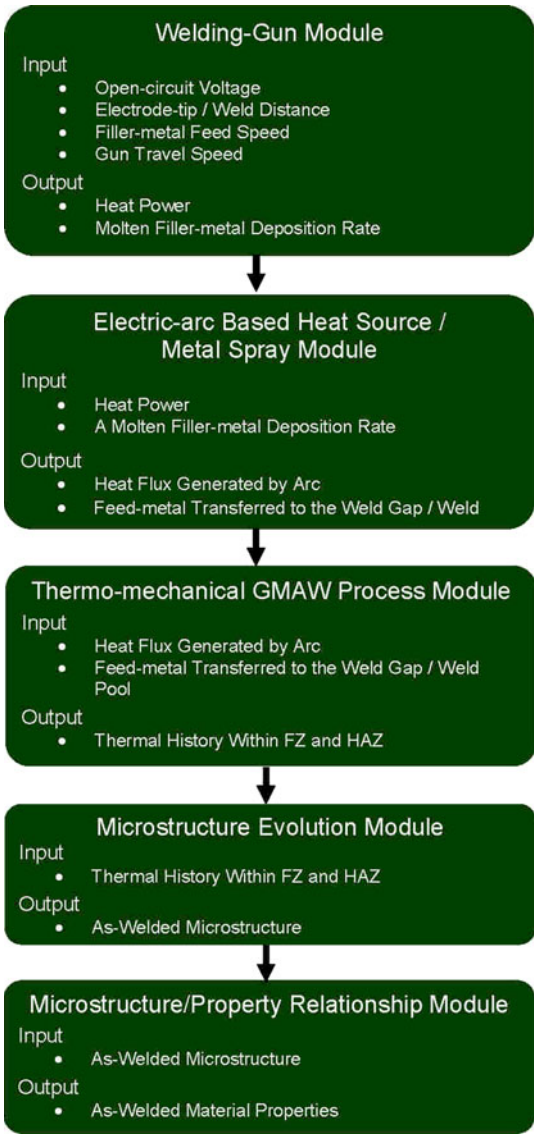

Fig. 2 The structure of the newly proposed multiphysics GMAW process model consisting of five modules

feed-metal deposition/spray rate over the weld-pool surface. Various experimental studies (Ref 32) have clearly established that heat flux and feed-metal deposition rate distributions are of a normal-circular type. This form of the heat flux and feed-metal deposition rate distributions will be adopted in this study. Accordingly, the heat flux distribution $q(r)$ as a function of the radial distance from the arc axis, r, is given as

$$q(r) = q_0 \exp\left(\frac{-r^2}{r_\sigma^2}\right), \qquad \text{(Eq 1)}$$

where $q(0)$ is the heat flux peak value while r_σ is a measure of the width of the power-density distribution function. A schematic of the $q(r)$ versus r function with $q(0) = 1$ and $r_\sigma = 1/3$ is depicted in Fig. 3.

$q(r)$ as given by Eq 1 contains two parameters, $q(0)$ and r_σ, and they are mutually related by the constraint that the surface integral of $q(r)$ with r ranging from zero to infinity must be equal to the arc-based total heat input power, as yielded by the welding-gun module. In other words,

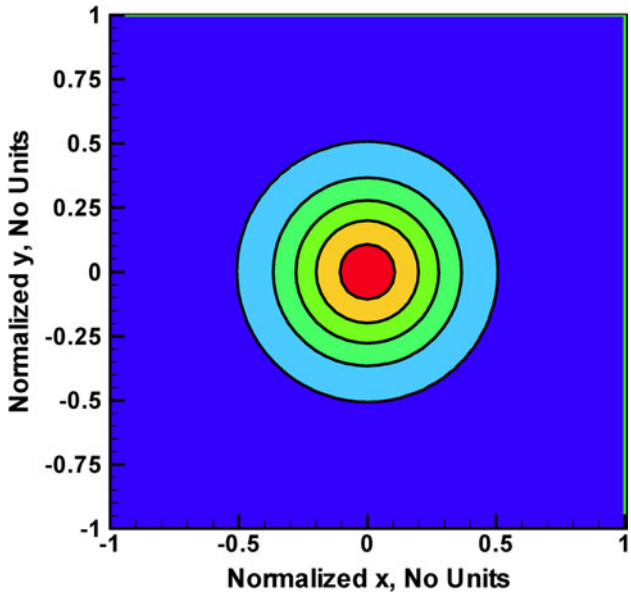

Fig. 3 A schematic representation of the heat flux circular-normal distribution function

$$\int_0^\pi q(r)\, 2\pi\, r\, dr = \int_0^\infty q_0 \exp\left(\frac{-r^2}{r_\sigma^2}\right) 2\pi\, r\, dr = q_0 \pi\, r_\sigma^2 = \eta\, V\, I, \qquad \text{(Eq 2)}$$

where η is the welding-gun power efficiency, V is the output voltage, and I is the output current.

The second relationship between $q(0)$ and r_σ, and thus the final parameterization/calibration of Eq 1, is typically done using a purely experimental/empirical approach, e.g., application of infra-red surface thermometry (Ref 33).

As far as the surface distribution of the feed-metal deposition rate is concerned, it is given by a two-parameter equation analogous to Eq 1. In this case, the two parameters are constrained by the fact that the integral of the corresponding distribution function for r ranging between zero and infinity must be equal to the total molten filler-metal deposition rate (as output by the welding-gun module). As in the previous case, the second functional relationship between the two parameters is obtained and the molten filler-metal deposition rate distribution function established using an experimental procedure within which the surface profile of the weld bead is characterized.

2.3 Thermomechanical GMAW Process Module

Within this module, the heat flux and mass flux distribution functions yielded by the electric-arc-based heat source/metal spray module are used as boundary conditions within a transient fully coupled thermomechanical finite-element GMAW process analysis. This analysis is effectively an adaptation of an FSW process model reported in our recent work (Ref 34-42). In the remainder of this section, a brief overview is provided by the key aspects of the thermomechanical GMAW process module, such as: (a) geometrical model; (b) meshed model; (c) computational algorithm; (d) initial conditions; (e) boundary conditions; (f) mesh sensitivity; (g) material model; and (h) computational tool.

2.3.1 Geometrical Model. The computational domain comprising two workpieces to be butt-welded initially (i.e., before welding) possessed a rectangular-parallelepiped shape with the following dimensions: (60 mm × 60 mm × 10 mm). The axes of the parallelepiped are aligned with the global *x*-*y*-*z* Cartesian system, as indicated in Fig. 4(a). The following orientation of the computational domain is chosen: (i) the weld contact interface is set orthogonal to the *x*-axis; (ii) the weld gun travel direction is aligned with the *y*-axis; while (iii) the workpiece through-the-thickness upward normal direction is aligned with the *z*-axis. The origin of the coordinate system ($x = y = z = 0$) is placed at the mid-value of *x*, minimum value of *y*, and at the minimum value of *z* of the computational domain.

To geometrically model the FZ, a different approach was adopted from that used in Ref 5, 6. In Ref 5, 6: (a) a V-shaped through-the-thickness groove centered at $x = 0$ and extending along the *y*-axis was created initially by removing the associated workpiece material from the two workpieces to be butt-welded; (b) to mimic groove filling during the GMAW process in the spray metal-transfer mode, the removed material was then progressively added in the *y*-direction (to track the motion of the welding-gun); and (c) extra material was added during the groove filling process to form the weld bead. This procedure effectively predefined the size of the FZ, i.e., the FZ was allowed to reside only within the groove. In this study, the size of the FZ was not predefined but was rather a result of the thermal interaction between the electric arc and the workpieces to be joined. In other words, the computed liquidus-temperature isosurface was used to define the FZ/HAZ boundary. To account for the filler-material deposited into the weld-pool and the resulting formation of the weld bead, the top surface of the workpiece was dynamically reshaped in accordance with the advancement of the weld gun. The profile of the resulting weld bead is consistent with the spraying-rate normal distribution function, as discussed in section 2.2. The resulting geometry of the two workpieces to be butt-welded, at the instant when the weld gun has traveled half of the distance in the *y*-direction, is depicted in Fig. 4(a).

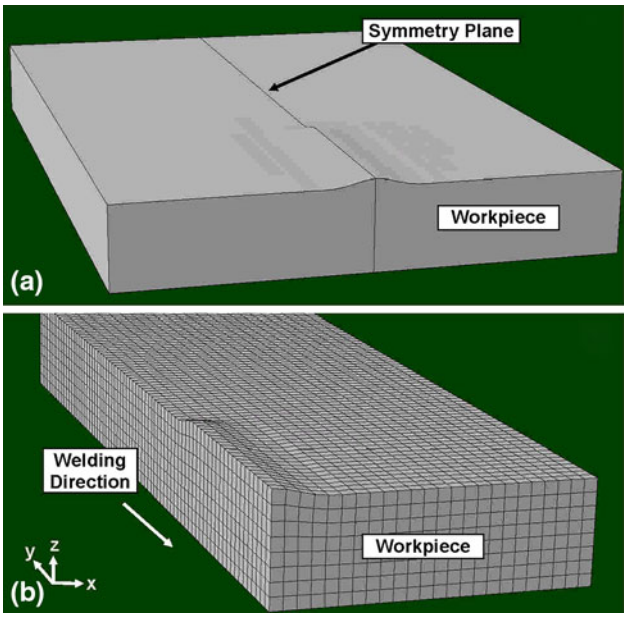

Fig. 4 Typical: (a) geometrical (after reflection across the weld boundary); and (b) meshed models used in the thermomechanical GMAW process module

It should be noted that the computational domain described above is symmetric about $x = 0$ and, hence, only one (right, when looking along the direction of motion of the welding-gun, in this study) half of this computational domain had to be explicitly analyzed.

2.3.2 Meshed Model. The selected half of the computational domain is meshed using between 16,425 and 52,429 eight-node, first-order, thermomechanically coupled, reduced-integration, hexahedral continuum elements. Figure 4(b) shows a close-up of the typical meshed model used in this study. Examination of this figure clearly reveals the presence of the deposited weld bead.

2.3.3 Computational Algorithm. All the calculations carried out within the present module are based on a transient, fully coupled, thermomechanical, unconditionally stable, implicit finite-element algorithm. At the beginning of the analysis, the computational domain is supported over its bottom ($z = 0$) face, made stress free, and placed at the ambient temperature. As welding proceeds, the electric-arc heat flux, represented by the radial normal distribution function, Eq 1, is applied to the top surface of the weldment and advanced in the welding (positive *y*) direction to track the position of the weld gun. Furthermore, in order to mimic additional thermal effects associated with the entry of the molten filler-material into the weld pool, a (volumetric) heat source described by a relation analogous to Eq 1 is introduced into the top layer of the workpiece elements and allowed to advance, at the welding speed, along the welding direction. Electromagnetic stirring was not modeled explicitly. Rather, its effect is implicitly accounted for by making the workpiece material acquire substantially higher values of the thermal conductivity at temperatures exceeding the liquidus temperature. Thermal interactions between the workpieces and the environment are handled by activating convection and radiation heat transfer modes, while heat transfer within the weldment including the FZ is assumed to take place via conduction. The resulting non-uniform thermal fields within the weldment are allowed to produce thermal stresses and, if sufficiently high, give rise to the local permanent deformations/distortions and residual stresses. In the cases when high thermal stresses caused the development of permanent distortions, following the standard practice, 95% of the work of plastic deformation was assumed to be dissipated in the form of heat while the remaining 5% was assumed to be stored in the form of local microstructural and crystal defects.

2.3.4 Initial Conditions. As mentioned above, the workpiece material is initially assumed to be at room/ambient temperature and stress free.

2.3.5 Boundary Conditions. Since only one half of the workpiece/weld assembly is explicitly analyzed, symmetry mechanical and thermal boundary conditions had to be applied across the $x = 0$ symmetry plane. As far as the additional mechanical boundary conditions are concerned, only the one associated with providing the support to the workpiece over its bottom face is applied. Regarding the additional thermal boundary conditions: (a) a radial normally distributed (moving) heat flux is applied over the top surface of the workpiece to mimic the interaction of the weld gun (advancing in the welding direction) and the weldment. It should be noted that, during GMAW, under certain welding conditions, motion of the weld gun and the associated non-uniformity of the weld current

can result in an unstable/periodic arc. These situations are not analyzed in this study, but could be readily accounted for by prescribing a periodic lateral displacement to the distributed flux described above; (b) natural convection and radiation boundary conditions are prescribed over all exposed surfaces of the workpiece/weld; and (c) the bottom surface is assumed to be insulated.

2.3.6 Mesh Sensitivity. In order to ensure that the key results and conclusions yielded by this study are not affected by the choice of the computational mesh, a mesh sensitivity analysis was carried out within which of progressively finer finite-element meshes are used. The selected finite-element mesh(es) represents a compromise obtained between the numerical accuracy and computational efficiency.

2.3.7 Material Model. It should be recognized that within the present multiphysics GMAW process model, thermomechanical and microstructural evolution aspects of the process are decoupled, i.e., treated separately. In other words, the thermomechanical GMAW process model was used in this study mainly to generate thermal histories of the material points and final strain/stress fields within the FZ and HAZ, while neglecting the contribution of various phase transformations and microstructure-evolution processes to the thermal and mechanical response of the material within the weld region. The resulting thermal histories of the material points within the weld region are then used in the (next) microstructure evolution module in order to determine the role of various phase transformations on the local distribution of the material microstructure within the weld region. In addition, the predicted stress/strain fields are used in the (last) microstructure/property relationship module.

In accordance with the discussion given above, the workpiece material and the filler-metal (assumed to be chemically identical to the workpiece material) are assumed to be homogeneous, single-phase, and capable of undergoing liquid-to-solid phase transformation, but not any of the solid/solid phase transformations. Due to the identical chemistry of the workpiece material and the filler-metal, only one material model had to be constructed/utilized. However, due to the thermomechanical character of the finite-element analysis utilized, both thermal and mechanical aspects of the material had to be addressed. The thermal portion of the material model is defined using the: (a) material mass density, ρ, specific heat, C_p, and thermal conductivity, k, for the heat-conduction part of the model; (b) the heat transfer coefficient, h, and the sink temperature, T_{sink} (= T_{room}), for the natural-convection part of the model; and (c) emissivity, ε, and the ambient temperature, T_{amb}(= T_{room}), for the radiation part of the model.

As far as the material's mechanical response is concerned, it is assumed to be isotropic (linearly) elastic and (strain-hardenable, strain-rate sensitive, thermally softenable) plastic. In addition, it is assumed that this response can be mathematically represented using the Johnson-Cook material-model formulation (Ref 43).

Within the Johnson-Cook material-model, the purely elastic response of the material is defined using the generalized Hooke's law, while the elastic/plastic response of the material is described using the following three relations: (a) a *yield criterion*, i.e., a mathematical relation which defines the condition which must be satisfied for the onset (and continuation) of plastic deformation; (b) a *flow rule*, i.e., a mathematical relation which describes the rate of change of different plastic-strain components in the course of plastic deformation; and (c) a *constitutive law*, i.e., a mathematical relation which describes the changes in material strength as a function of the extent of plastic deformation, the rate of deformation, and temperature.

For MIL A46100, the material analyzed in this study, plastic deformation is considered to be of a purely distortional (volume-preserving) character and, consequently, the yield criterion and the flow rule are, respectively, defined using the von Mises yield criterion and a normality flow rule. The von Mises yield criterion states that the (von Mises) equivalent stress (a scalar related to the second invariant of the stress deviator) must be equal to the material yield strength for plastic deformation to occur/proceed. The normality flow-rule, on the other hand, states that the plastic flow takes place in the direction of the stress-gradient of the yield surface (a locus of the stress points within the associated multidimensional stress space at which the von Mises stress criterion is satisfied). The Johnson-Cook strength constitutive law used is defined as:

$$\sigma_y = A\left[1 + \frac{B}{A}(\bar{\varepsilon}^{pl})^n\right]\left[1 + C\log(\dot{\bar{\varepsilon}}^{pl}/\dot{\bar{\varepsilon}}_0^{pl})\right]\left[1 - T_H^m\right], \qquad \text{(Eq 3)}$$

where $\bar{\varepsilon}^{pl}$ is the equivalent plastic strain, $\dot{\bar{\varepsilon}}^{pl}$ the equivalent plastic strain rate, $\dot{\bar{\varepsilon}}_0^{pl}$ a reference equivalent plastic strain rate, A the zero-plastic-strain, reference-plastic-strain-rate, room-temperature yield strength, B the strain-hardening constant, n the strain-hardening exponent, C the strain-rate constant, m the thermal-softening exponent, and $T_H = (T - T_{room})/(T_{melt} - T_{room})$ a room-temperature (T_{room}) based homologous temperature while T_{melt} is the melting (or more precisely, solidus) temperature. All temperatures are given in Kelvin. In Eq 3, the parameter A defines the as-received material yield strength, the term within the first pair of brackets defines the effect of additional strain hardening, the term within the second pair of brackets quantifies the effect of deformation rate while the last term shows the reversible effect of temperature. Examination of Eq 3 reveals that, at temperatures $T \geq T_{melt}$, material strength drops to zero, i.e., the material undergoes melting. However, due to the reversible character of the last term on the right-hand side of Eq 3, material strength is restored upon solidification ($T < T_{melt}$).

As far as the coupled thermomechanical response of the material is concerned, it is quantified using a single parameter, i.e., the coefficient of linear thermal expansion α.

Tables 1 and 2 provide a summary of the values for all the MIL A46100 thermal, mechanical, and thermomechanical model parameters used in this study. It should be noted that the values for the material-property parameters listed in these tables correspond to their prototypical counterparts observed in the as-received condition of MIL A46100. During the GMAW process, material microstructure and properties change within the weld and the HAZs. The effect of these changes in the material microstructure and properties on the spatial distribution and temporal evolution of the thermomechanical fields within the weld can be assessed by coupling, in real-time, the microstructure-evolution and microstructure/property-relationship modules (presented next). However, at this stage of the GMAW-process model development, this coupling was not undertaken. Instead, the microstructure-evolution and microstructure/property-relationship modules utilized thermomechanical fields produced by the thermomechanical module based on the material properties in the as-received condition of MIL A46100. This shortcoming of the present GMAW-process model is being addressed in this study, and will be reported in a future communication.

Table 1 Johnson-Cook Strength Model Material Parameters for MIL A46100

Parameter	Symbol	Units	Value
Young's modulus	E	GPa	205-215
Poisson's ratio	v	N/A	0.285-0.295
Reference strength	A	MPa	1000-1100
Strain-hardening parameter	B	MPa	250.0
Strain-hardening exponent	n	N/A	0.12
Strain-rate coefficient	C	N/A	0.02
Room temperature	T_{room}	K	298.0
Melting temperature	T_{melt}	K	1720
Temperature exponent	m	N/A	0.5

Table 2 General, thermomechanical, and thermal parameters for MIL A46100

Parameter	Symbol	Units	Value
Material mass density	ρ	kg/m^3	7840-7860
Coefficient of linear thermal expansion	α	1/K	11e−6-12e−6
Specific heat	C_p	J/kg K	440-520
Thermal conductivity	k	W/m K	35-50
Heat transfer coefficient	h	W/m^2 K	45
Sink temperature	T_{sink}	K	298
Emissivity	ε	N/A	0.57
Ambient temperature	T_{amb}	K	298

2.3.8 Computational Tool. The thermomechanical GMAW process module is executed using an implicit solution algorithm implemented in ABAQUS/Standard, a general-purpose finite-element solver (Ref 44). In addition, to account for the spatially non-uniform and time-varying heat flux, *DFLUX* user subroutine was used. This general-purpose subroutine enables the user to define non-uniform distributed flux in a heat transfer or mass diffusion analysis.

2.4 Microstructure Evolution Module

While the computational procedure to be presented in this section is applicable to any type of steel, as well as across the whole class of metallic materials, its development and application will be closely tied to MIL A46100. Consequently, a brief introduction to this material is given at the beginning of this section.

2.4.1 Introduction to MIL A46100. MIL A46100 is a rolled homogenous armor (RHA) plain steel whose chemical composition, material processing, and plate-fabrication routes as well as the resulting material-microstructure and properties are governed by the specification MIL STD A-46100 (Ref 45). This steel falls into the category of air-quenchable, self-tempered, high-hardness, low-alloy martensitic steels. The name RHA is used to denote that plates of this material (used in light-armor applications) are produced by hot rolling steel castings and during this process material microstructure is homogenized while most of the microstructural imperfections/defects are removed.

In this study, a detailed overview was presented of the chemical composition, typical properties, and the weldability and common welding practice associated with MIL A46100. Consequently, these aspects of this material will not be presented in this article.

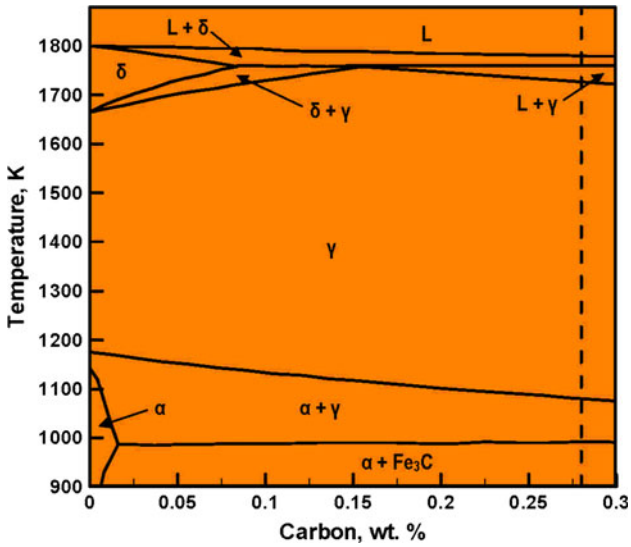

Fig. 5 A portion of the quasi-binary para-equilibrium Fe-C phase diagram corresponding to the non-carbon alloy additions at a level nominally found in MIL A46100

2.4.2 MIL A46100 Phase Diagram. Following the standard practice, the equilibrium state of MIL A46100 (as defined by the crystalline phases present, their chemical compositions, and their volume fractions) at different temperatures (and under atmospheric pressure) can be determined using the corresponding multicomponent (equilibrium) phase diagram. In this diagram, the axes are the concentrations of all the MIL A46100 main alloying elements (i.e., C, Mn, Si, Cr, Mo, etc.) and temperature. However, the utility of such a multicomponent phase diagram is limited due to its multidimensional nature. Instead, the corresponding "*quasi-binary*" para-equilibrium Fe-C phase diagram is typically used. Within this two-dimensional, alloy-system-dependent diagram, it is assumed that the concentration of each non-carbon alloying element is the same as that in the overall material itself. In other words, it is assumed that due to the low diffusivity of the non-carbon alloying elements relative to that of carbon, their partitioning between various phases does not take place. The quasi-binary para-equilibrium phase diagram of MIL A46100 is displayed in Fig. 5. Examination of Fig. 5 reveals that the MIL A46100 quasi-binary phase diagram is quite similar to the true-binary Fe-C phase diagram, except that the values of the characteristic temperatures and concentrations have been slightly modified (due to the low-alloy character of MIL A46100). It should be noted, however, that there are additional phases such as Mo_2C, $(Cr,Mo)_{23}C_6$, and (Ti,V)N which were not shown in the quasi-binary phase diagram. The omission of these phases from the phase diagram is done deliberately in order to keep the diagram simple and is justified by the fact that the volume fraction of these phases is quite small.

Since partitioning of alloying elements does take place in MIL A46100, the quasi-binary phase diagram displayed in Fig. 5 has relatively limited utility. On the other hand, while, as pointed out earlier, there are challenges associated with the graphical representation of a multicomponent phase diagram, one can extract and readily display specific details contained within the phase diagram. For example, for the steel in question, one can compute the equilibrium volume fraction of all the phases present at different temperatures and the

atmospheric pressure. This was done in Ref 30 using the materials-thermodynamics commercial software ThermoCalc (Ref 46) and the results of this calculation are shown in Fig. 6(a) and (b). Examination of Fig. 6(a) enables the determination of the following MIL A46100 characteristic temperatures: (a) the liquidus temperature (= 1772 K), defined as the temperature at which the volume fraction of the liquid first begins to deviate from 100% during cooling; (b) the peritectic-transformation temperature (= 1750 K), defined as the temperature at which austenite first appears during cooling; (c) the solidus temperature (= 1720 K), defined as the lowest temperature at which the liquid is still present; (d) the Ac_3 temperature (= 1076 K), defined as the temperature at which α-ferrite first appears during cooling; and (e) the Ac_1 temperature (= 982 K), defined as the temperature at which austenite vanishes during cooling. On the other hand, examination of Fig. 6(b) reveals that: (a) (Ti,V)(N,C) primary precipitates first appear at temperatures slightly above the solidus temperature, due to the associated high super-saturation of the residual liquid with the alloying elements, and the precipitate volume fraction does not change significantly during subsequent cooling; and (b) in addition, it is seen that cementite begins to form during cooling at a temperature in the Ac_1-Ac_3 range while MoC forms at temperatures below Ac_1.

2.4.3 Time-Temperature-Transformation (TTT) Diagram(s). As mentioned earlier, during cooling of the material within the FZ, austenite (a high-temperature γ-phase with face-centered-cubic, FCC crystal structure) undergoes transformation into a number of low-temperature ferrite (a low-temperature α-phase with body-centered-cubic, BCC crystal structure) based phases/microconstituents. Some of these transformations are not predicted by the phase diagram since they occur under non-equilibrium finite cooling-rate conditions while the phase diagram predicts the state of the material only under extremely slow cooling (i.e., equilibrium) conditions. To overcome this shortcoming of the phase diagram, additional, material-specific time-based diagrams are used. The first diagram of this kind is the so-called "TTT" diagram. A series of TTT diagrams for MIL A46100, as a function of the maximum temperature experienced by austenite, is depicted in Fig. 7(a) to (e). In general, diagrams of this type are constructed experimentally by quenching the steel in question from a temperature greater than Ac_1 to (and holding at) a desired temperature below Ac_1 and determining the time of the onset of austenite decomposition, the so-called "incubation time." Major advances have been made in the capabilities of the computational methods and tools used for the construction of fairly accurate TTT diagrams. For example, the TTT diagrams displayed in Fig. 7(a) to (e) were determined computationally in Ref 30 using a proprietary computer code.

The TTT diagrams displayed in Fig. 7(a) to (e) are adopted in this study. The (missing) TTT diagrams associated with the pre-quench austenite temperatures other than the ones referenced in Fig. 7(a) to (e) are obtained using a simple linear interpolation scheme. Examination of the TTT diagrams displayed in Fig. 7(a) to (e) reveals the presence of three (complete or partial) C-shaped curves. The two high-temperature curves labeled F_s and F_f represent, respectively, the loci of the incubation times for the allotriomorphic ferrite (a variation of ferrite possessing a featureless external morphology which does not reflect the symmetry of the associated underlying crystalline structure) and acicular/Widmanstatten ferrite (a version of ferrite possessing an acicular/lenticular-plate morphology which grows

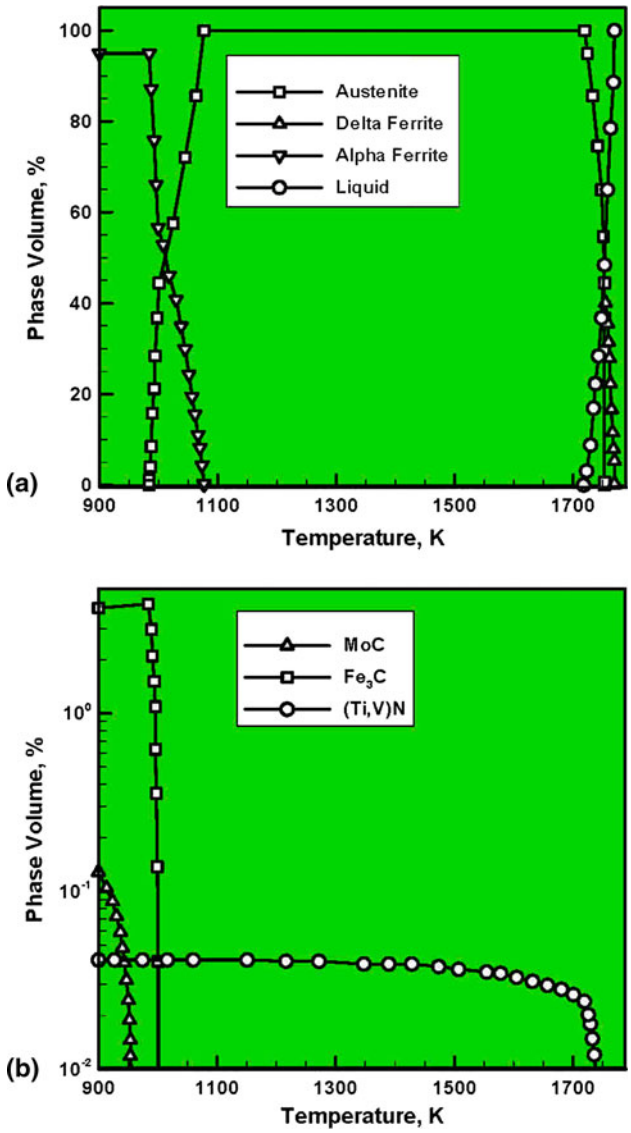

Fig. 6 Equilibrium volume fractions of all the phases present in MIL A46100 as a function of temperature (and at atmospheric pressure) (Ref 30)

into the untransformed austenite from the austenite/austenite grain boundaries and/or allotriomorphic-ferrite/austenite interfaces). The lower C-shaped curve, B_s, is associated with the displacive bainitic phase transformation which produces a lath or acicular-shaped bainitic phase in which atomic diffusion of iron and alloying elements other than carbon is suppressed. Further examination of Fig. 7(a) to (e) reveals the presence of two low-temperature horizontal lines. These lines, labeled as M_s and M_f, denote, respectively, the temperatures at which displacive/diffusionless martensitic phase transformation starts and finishes. The product of this transformation is martensite, a solid solution with a highly distorted tetragonal crystal structure (due to high levels of carbon super-saturation) and acicular morphology. Lastly, it is seen that Fig. 7(a) to (e) contains two high-temperature horizontal lines. These lines, labeled as Ac_1 and Ac_3, represent the highest temperature at which, during cooling, austenite volume fraction decreases below 1.0 and the highest temperature at which austenite volume fraction drops to 0.0, respectively.

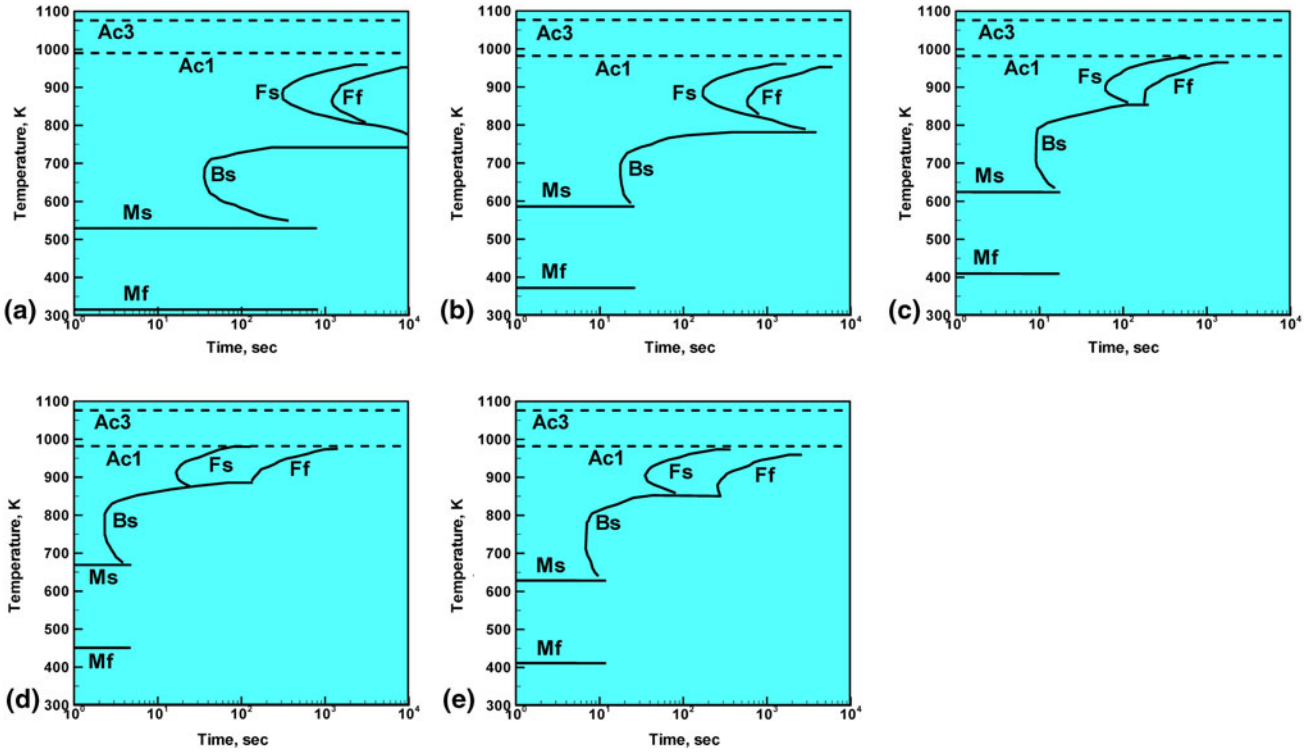

Fig. 7 The TTT diagrams for MIL A46100 steel equilibrated initially at: (a) 993 K; (b) 1003 K; (c) 1053 K; (d) 1076 K; and (e) 1330 K. Symbols F_s, F_f, and B_s are used to denote the locus of the temperature vs. time conditions at which austenite begins to transform, respectively, into allotropic ferrite, acicular ferrite, and bainite. Symbols Ac_3, Ac_1, M_s, and M_f have their common meanings (please see text for details) (Ref 30)

2.4.4 Continuous-Cooling-Transformation (CCT) Diagram(s). As pointed out above, a TTT diagram is obtained under particular thermal-history conditions which include quenching of austenite from a super-Ac_1 temperature to (and holding at) a sub-Ac_1 temperature until the associated austenite-decomposition phase transformation begins to take place. Within an actual GMAW process, no material point within the weld region is generally expected to be associated with this type of thermal history. Instead, one would typically expect a thermal history which is characterized by (initial fast heating and subsequent) continuous cooling from the maximum temperature to which austenite has been subjected. Thus, a diagram is needed which can be used to display various types of austenite-decomposition phase transformations under arbitrary continuous-cooling conditions. In order to determine the non-isothermal incubation time, for austenite decomposition during continuous-cooling, the so-called Scheil additive rule is adopted in this study. The Scheil additive rule simply postulates that the material has to reach the same critical state of incubation for the particular austenite-decomposition phase-transformation to begin. Since a detailed overview of the Scheil rule was given in our recent work (Ref 6), it will not be discussed here any further.

Application of the Scheil additive rule to MIL A46100 yielded the CCT diagram displayed in Fig. 8. The diagram displayed in Fig. 8 is obtained under particular continuous-cooling conditions, i.e., the ones associated with constant cooling rates. It should be noted that both TTT and CCT curves are shown in Fig. 8 and, for improved clarity, the TTT curves are denoted in this figure using dashed lines. For the same reason, the resulting CCT curves are drawn as heavy lines, while representative cooling curves are denoted as light solid lines. It should be noted that, due to the athermal nature of the martensitic transformation, the M_s transformation temperature is not affected by the details of the material cooling history. Consequently, the M_s and M_f horizontal lines coincide with their TTT counterparts.

2.4.5 GMAW Weld Zones. As mentioned earlier, a GMAW weld region typically consists of two main zones: (a) the FZ containing a mixture of the base and filler-metals; and (b) the HAZ containing the work-piece base metal which remains in the solid state but may undergo significant microstructural changes during welding, as shown schematically in Fig. 9. The HAZ itself can be divided into several sub-zones. Moving outward from the weld centerline, the following sub-zones are typically observed: (i) the coarse-grained sub-zone, which mainly contains martensite. The prior austenite grain size in this region is quite large due to steel exposure to very high temperatures (within the single-phase austenite region); (ii) the fine-grained sub-zone, which contains martensite and bainite, formed during cooling, from austenite with a relatively smaller grain size due to its exposure to lower temperatures (within the single-phase austenite region); (iii) the so-called inter-critical sub-zone, within which the base-metal is exposed to temperatures sufficiently high to form austenite but not high enough to fully austenitize the material. Consequently, this sub-zone contains both non-austenite phases (i.e., ferrite and alloy-carbides) present at the highest temperature to which this sub-zone was exposed and the products of austenite decomposition during cooling (i.e., martensite, bainite, ferrite); and (iv) the so-called sub-critical zone, within which the material was never exposed to a temperature sufficiently high to

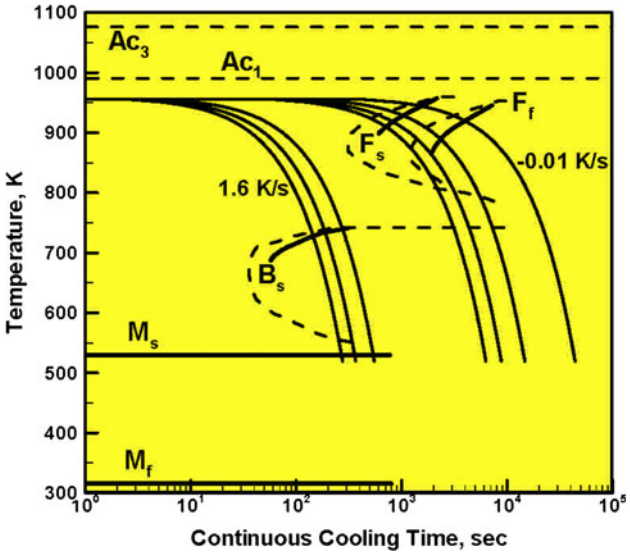

Fig. 8 MIL A46100 CCT diagram corresponding to the TTT diagram displayed in Figure 7(a): CCT curves and the M_s and M_f temperature lines are denoted using heavy solid lines, while representative cooling curves are shown as light solid lines. The TTT curves and the Ac_1 and Ac_3 temperature lines are denoted using dashed lines

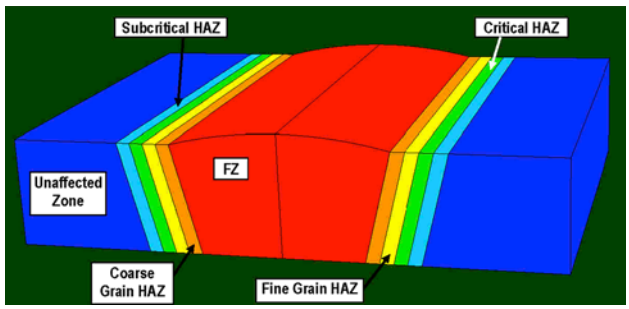

Fig. 9 A schematic of the typical GMAW process zones and subzones: FZ = Fusion Zone and HAZ = Heat-Affected Zone

result in the formation of austenite. However, the maximum temperature experienced by the material in this sub-zone is sufficiently high to cause martensite tempering (i.e., formation of a mixture of ferrite and fine carbide particles).

2.4.6 Microstructure Evolution Within the FZ. It should be noted that the computational procedure used to construct the TTT and CCT diagrams could be used to predict the incubation time for austenite decomposition under an arbitrary thermal history. However, additional modeling and simulation procedures are needed to predict further progress of various austenite-decomposition reactions (and the corresponding volume fractions of the transformation products). Such procedures are developed in this section for the FZ material points. In the next section, the corresponding models will be presented for the HAZ material points. Two sets of models were deemed necessary, considering the fact that the material points within the FZ and the HAZ generally possess quite different thermal histories. That is, within the FZ thermal history is dominated by the continuous cooling of austenite (formed from the liquid phase during solidification), while within the HAZ thermal history involves initial heating of the as-received martensitic microstructure and subsequent cooling of the austenite phase (formed from the martensitic phase during heating).

As mentioned earlier, within the FZ, depending on the cooling history, austenite may transform into one or more of the following phases: allotriomorphic ferrite, acicular ferrite, bainite, and/or martensite. In the remainder of this section, procedures are presented for computing the final volume fractions of the phases formed during austenite decomposition within different portions of the FZ.

Allotriomorphic-Ferrite Volume Fraction. Austenite grains formed during solidification are, for the most part, of a columnar shape and aligned with the direction of the maximum heat extraction. For modeling purposes, the cross section of the columnar austenite grains is typically idealized as being of a regular hexagonal shape. In other words, as shown schematically in Fig. 10(a), the columnar austenite grains are assumed to form a perfect honeycomb structure, with the axes of the hexagonal prisms being aligned with the local maximum heat-extraction direction. In addition to specifying the shape of the austenite grains, the hexagonal-section edge length, a, must be specified since, as will be shown below, it affects the final volume fraction of the allotriomorphic ferrite. The hexagonal-section edge length is, in turn, mainly affected by the maximum local cooling rate attained by the liquid during solidification. Specifically, a decreases with an increase in the maximum local cooling rate of the melt during solidification. To establish functional relationship between the austenite-grain cross-sectional area and the local solidification conditions, one must model explicitly melt-solidification aspects of the GMAW process. Since this type of modeling is beyond the scope of the present effort, the initial distribution of the austenite grain size within the FZ could not be carried out. Instead, a prototypical value of $a = 50$ μm was used throughout the entire FZ (Ref 47).

The allotriomorphic ferrite growth model utilized in this study was developed in our recent work (Ref 5) and will be reviewed briefly below. The model is based on the following postulates: (a) a parabolic relationship exists between the allotriomorphic-ferrite thickness growth rate, dq/dt, and the instantaneous ferrite-plate thickness, q, as:

$$\frac{dq}{dt} = \frac{\alpha_1(t)}{q}, \qquad \text{(Eq 4)}$$

where $\alpha_1(t)$ is a one-dimensional temperature-dependent parabolic-growth-rate constant; (b) the allotriomorphic ferrite finite-plate thickness, q_f, can be obtained by integrating of Eq 4 between the time at which the growth starts, t_i, and the time at which the growth ceases, t_f, along the given temperature history, $T(t')$, as:

$$q_f = 0.5 \int_{t_i}^{t_f} \alpha_1(T(t'))t'^{-0.5}dt'. \qquad \text{(Eq 5)}$$

In Eq 5, for any austenite cooling history, time t_i (and the associated γ-austenite → allotriomorphic ferrite phase transformation-start temperature) are obtained using the aforementioned CCT procedure and the F_s-labeled, C-shaped curve in Fig. 7 and 8. On the other hand, t_f (and the associated γ-austenite → allotriomorphic ferrite phase transformation-end temperature) is determined using the same procedure, but by employing F_f or B_s C-shaped curves. In other words, transformation of austenite into allotriomorphic ferrite is

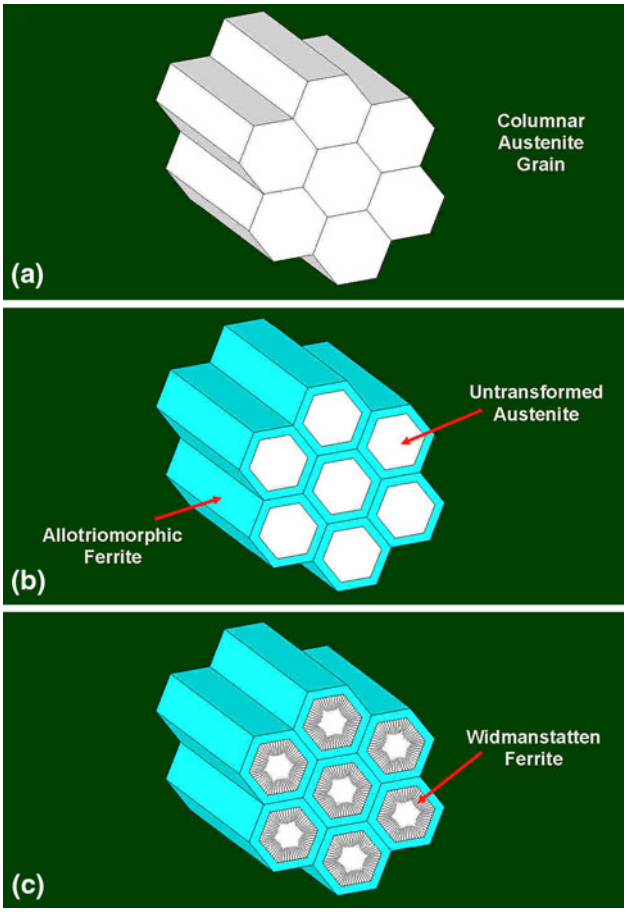

Fig. 10 Schematic representations of the columnar-grain microstructure in: (a) untransformed austenite; (b) austenite partially transformed into allotriomorphic ferrite; and (c) austenite partially transformed into allotriomorphic and Widmanstatten ferrite

assumed to cease once kinetically superior austenite → Widmanstatten ferrite or austenite → bainite phase transformations initiate; (c) value of the parabolic-growth rate constant is assumed to be controlled by carbon diffusion within austenite from the advancing allotriomorphic growth front. In other words, following the experimental investigation reported in Ref 7, it is assumed that para-equilibrium conditions exist during the austenite → allotriomorphic ferrite transformation. Using available experimental data (Ref 7, 47), a functional relationship is established between α_1 and temperature in MIL A46100 and this functional relationship is depicted in Fig. 11. Examination of this figure reveals that, as the temperature decreases, α_1 first increases as a result of an increased thermodynamic driving force for the austenite → allotriomorphic ferrite transformation. On the other hand, at sufficiently low temperatures, the diffusivity of carbon becomes quite low, so that transformation of austenite → allotriomorphic ferrite becomes kinetically constrained, causing a reduction in α_1; and (d) finally, it is assumed that a functional relationship can be established between the allotriomorphic ferrite plate thickness, q_f, and its volume fraction, $V_{\alpha A}$. This functional relationship is inferred by applying a simple geometrical computational procedure to the schematic displayed in Fig. 10(b) which depicts a partially transformed section of austenite. The resulting functional relationship can be stated as:

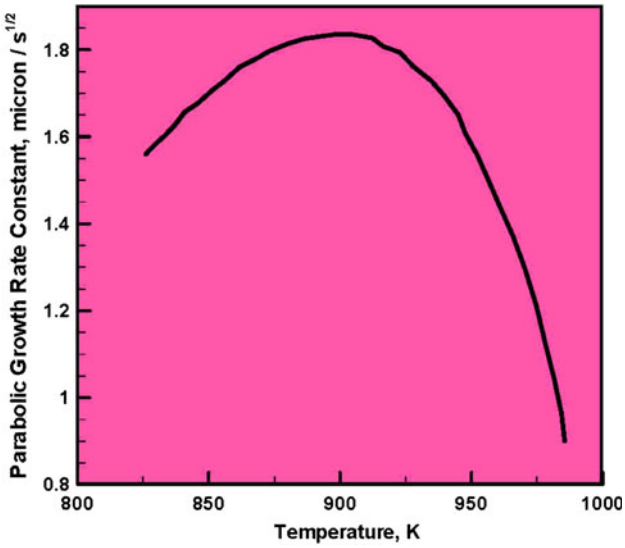

Fig. 11 Temperature dependence of the one-dimensional parabolic growth rate constant for the austenite → allotriomorphic ferrite phase transformation in MIL A46100 (Ref 47)

$$V_{\alpha A} = \frac{[2q_f \tan(30^\circ)(2a - 2q_f \tan(30^\circ))]}{a^2}. \quad \text{(Eq 6)}$$

Widmanstatten-Ferrite Volume Fraction. Examination of Fig. 8 reveals that, at relatively high transformation temperatures, the onset of austenite to Widmanstatten ferrite phase transformation causes the kinetically sluggish austenite to allotriomorphic ferrite transformation to cease. Following a detailed analysis presented in our recent work (Ref 5), the growth rate of the Widmanstatten ferrite is assumed to be controlled by the rate of lengthening of this lens-shaped phase in a direction normal to the local allotriomorphic ferrite/austenite interface. To help clarify geometrical/topological details related to the formation of Widmanstatten-ferrite, a simple schematic of partially transformed austenite grains is depicted in Fig. 10(c). Examination of this figure reveals the presence of prior austenite grain-boundary regions which have been transformed into allotriomorphic ferrite, as well as lenticular-shaped Widmanstatten plates advancing from the allotriomorphic ferrite/austenite interfaces toward the untransformed austenite grain centers.

As discussed in great detail in our recent work (Ref 5), the rate of the austenite → Widmanstatten-ferrite phase transformation is affected not only by the para-equilibrium condition still present at the ferrite advancing front and the associated carbon diffusion from this front into the untransformed austenite, but also by the displacive character of the austenite to Widmanstatten ferrite transformation. Following the procedure described in Ref 10, 48, which is based on the calculation of the Widmanstatten-ferrite area fraction within the austenite grains with hexagonal cross-section, Fig. 10(c), the following expression is derived for computing the Widmanstatten-ferrite volume fraction, $V_{\alpha W}$:

$$V_{\alpha W} = C_4 G \left[\frac{2a - 4q_f \tan(30^\circ)\, t_{\alpha W}^2}{(2a)^2}\right], \quad \text{(Eq 7)}$$

where C_4 [= 7.367 s^{-1} (Ref 19)] is an alloy-composition independent constant, G [= 52 μm/s (Ref 47)] is the Widmanstatten

ferrite lengthening rate, and $t_{\alpha W}$ is the total time available for the austenite → Widmanstatten ferrite transformation (it should be recalled that once temperature drops below B_S, the austenite → Widmanstatten ferrite transformation ceases and it is replaced with a austenite → bainite phase transformation).

Volume Fraction of Bainite. As mentioned earlier, bainite is a product of austenite-decomposition and the austenite → bainite phase-transformation is of a displacive character but its progress is controlled by a carbon diffusion into the untransformed austenite matrix. As established in a series of publications by Bhadeshia and co-workers (Ref 47-49), growth of bainite involves three distinct processes: (a) nucleation and lengthening of bainite platelets (commonly referred to as subunits) at austenite grain boundaries and phase interfaces. Upon reaching a critical size, lengthening of the bainite subunits is arrested by the plastic deformation accumulated within the surrounding austenite; (b) the transformation then proceeds by nucleation of new subunits ahead of the arrested ones. The newly formed subunits also become arrested and this sequence of processes continues; and (c) the result of the sequential nucleation of bainite subunits is the formation of unit clusters commonly referred to as "*sheaves*." It is the rate of lengthening of the sheaves which controls the overall progress of the austenite → bainite phase transformation. A schematic of the bainite-formation mechanism just described is given in Fig. 12.

To determine the rate of the bainitic transformation (and the associated increase in the bainite volume fraction) as a function of time, temperature, chemical composition (and austenite grain size), the model proposed by Matsuda and Bhadeshia (Ref 49) was utilized. This model was fully validated in Ref 49 by comparing its predictions with published isothermal and continuous cooling transformation results. Within this quite elaborate model, the overall rate of increase of the bainite volume fraction is related to the three aforementioned basic processes, and each of these processes is analyzed in great detail. Due to space limitations, details of the model could not be reproduced here. Instead, Fig. 13 shows a set of constant cooling curves which relate the volume fraction of bainite to the instantaneous temperature for the MIL A46100 HAZ section which was described using TTT and CCT diagrams displayed in Fig. 7(a) and 8, respectively. By employing a procedure similar to that described in the case of the allotriomorphic ferrite, the results displayed in Fig. 13 are used in this study to construct a bainite evolution algorithm under arbitrary thermal-history conditions.

Volume Fraction of Martensite. When the temperature drops to M_s all the aforementioned austenite-decomposition phase-transformations are assumed to cease and to be replaced with the kinetically superior diffusionless austenite → martensite phase transformation. This transformation is of an athermal character, i.e., the extent of this transformation depends only on temperature (within the M_s-M_f range) and not on time. Since, as confirmed by the TTT diagrams displayed in Fig. 7(a) to (e), M_f is above the room temperature, martensitic transformation is expected to cause a complete transformation of austenite. Thus, the volume fraction of martensite, V_{Ms}, can be computed by simply subtracting the sum of volume fractions of all the room-temperature phases from 1.0.

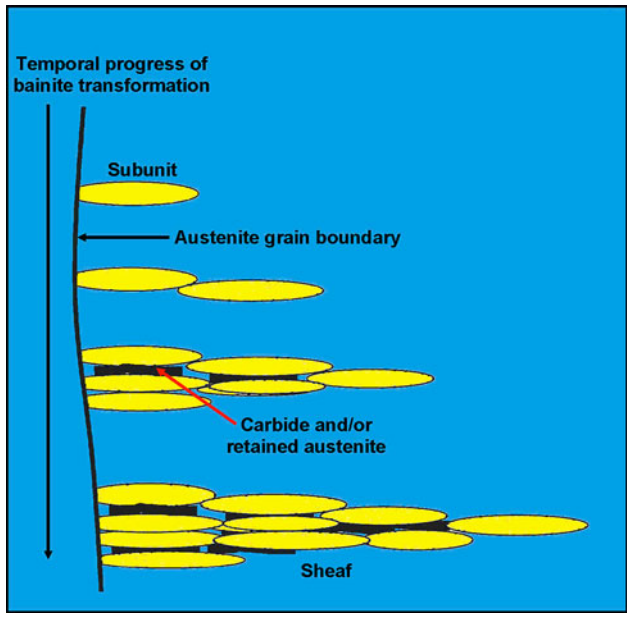

Fig. 12 Schematic of the bainite growth mechanism via the nucleation of sub-units, their growth and arrest, and subsequent autocatalytic nucleation of new sub-units (resulting in the formation of sub-unit clusters commonly referred to as sheaves) (Ref 49)

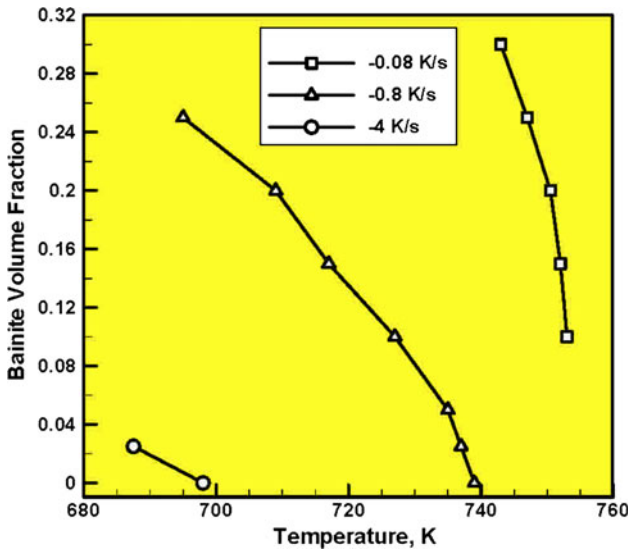

Fig. 13 The effect of transformation temperature and (constant) cooling rate on the progress of austenite → bainite martensitic transformation, in the case of austenite with the TTT and CCT diagrams corresponding to those shown in Fig. 7(a) and 8, respectively

Volume Fraction of Other Crystalline Phases. As established above, complete transformation of austenite to martensite is predicted and, hence, no retained austenite is expected. Other potential phases present at room temperature are not related directly to decomposition of austenite, but rather the results of the precipitation reactions which take place once the solubility limit for austenite is exceeded, during cooling. In MIL A46100, these phases generally include (Ti, V)N and MoC. Room-temperature volume fractions of these phases are approximately predicted by the equilibrium phase diagram, Fig. 6(b).

2.4.7 Phase Volume Fractions Within the HAZ. As explained earlier, material points within the HAZ are subjected to more complicated thermal histories which include both heating and cooling portions. The HAZ is operationally defined as a region surrounding the FZ within which these thermal histories cause noticeable and significant changes in the weldment-material microstructure and properties. For convenience, changes in the HAZ material microstructure during heating and cooling portions of the thermal history are analyzed separately.

Heating Portion of the Thermal History. MIL A46100 in its as-received condition typically possesses an auto-tempered martensitic microstructure. The extent of changes in this microstructure within the HAZ is mainly a function of the maximum-exposure temperature (as well as the exposure time of the material to the highest temperatures). Specifically, if the maximum-exposure temperature never exceeds Ac_1, the only microstructural changes expected are those associated with tempering of martensite. The outcome of these microstructural changes is the formation of ferrite and, initially, ε-carbide (or, finally, alloyed cementite). On the other hand, when the maximum-exposure temperature exceeds Ac_1, formation of austenite at the prior-austenite grain boundary junctions takes place. A schematic of this martensite to austenite phase transformation is depicted in Fig. 14(a) and (b), in which elongated prior-austenite grains are shown in order to reveal the effect of hot-rolling on the material microstructure.

To model the carbide-precipitation reactions associated with martensite tempering and phase transformations associated with austenite formation from martensite, analogous approaches are used in this study. That is, in both cases it is assumed that the processes in question involve nucleation and subsequent growth of the product phases (under para-equilibrium conditions). The progress of these processes is represented mathematically using the so-called Kolmogorov-Johnson-Mehl-Avrami (KJMA) relation (Ref 50). In the case of an isothermal phase transformation, the KJMA relation can be expressed as:

$$V_\gamma = V_\gamma^{\mathrm{eq}}(1 - \exp[-\{k(T) \times t\}^n]), \qquad \text{(Eq 8)}$$

where V_γ and V_γ^{eq} represent, respectively, the product-phase current and equilibrium volume fractions, $k(T)$ is a nucleation/growth-rate-related kinetic parameter, t is the isothermal holding time at temperature T, and n [= 1.9 (Ref 7)] is a temperature-invariant exponent. Temperature dependence of k is normally defined using an Arrhenius-type relation in the form:

$$k(T) = k_0 \times \exp\left(-\frac{Q}{RT}\right), \qquad \text{(Eq 9)}$$

where k_0 is a pre-exponential constant, Q is an overall nucleation/growth activation energy for the ferrite to austenite phase transformation, while R is the universal gas constant. Using multiple-regression analysis and the relevant isothermal kinetics data, the KJMA parameters are determined as follows: (a) for the martensite/austenite transformation, $k_0 = 1.33 \times 10^5\ \mathrm{s}^{-1}$ (Ref 7), $Q = 117.07$ kJ/mol (Ref 7); and (b) for the martensite-tempering reaction, $k_0 = 4.10 \times 10^5\ \mathrm{s}^{-1}$ (Ref 51, 52), $Q = 115.50$ kJ/mol (Ref 51, 52).

It is clear that Eq 8 cannot be directly used in the analysis of microstructural changes within the HAZ, since the associated phase transformations proceed under continuous heating (and cooling) conditions, rather than under isothermal holding conditions. Instead, to overcome this problem, a local (continuous) thermal-history function $T(t)$ can be first approximated, as a sequence of N isothermal-holding steps each associated with a temperature T_i (i = 1, 2,…,N) and of a duration Δt. Then Eq 8 could be used to include the cumulative contributions of all the isothermal-transformation steps as:

$$V_\gamma(t(T_{\mathrm{N}})) = V_\gamma^{\mathrm{eq}}\left(1 - \exp\left[-\left\{\sum_{i=1}^{N} k(T_i) \times \Delta t\right\}^n\right]\right) = V_\gamma^{\mathrm{eq}}\left(1 - \exp\left[-\left\{\sum_{i=1}^{N} k_0 \times \exp\left(-\frac{Q}{RT_i}\right) \times \Delta t\right\}^n\right]\right). \qquad \text{(Eq 10)}$$

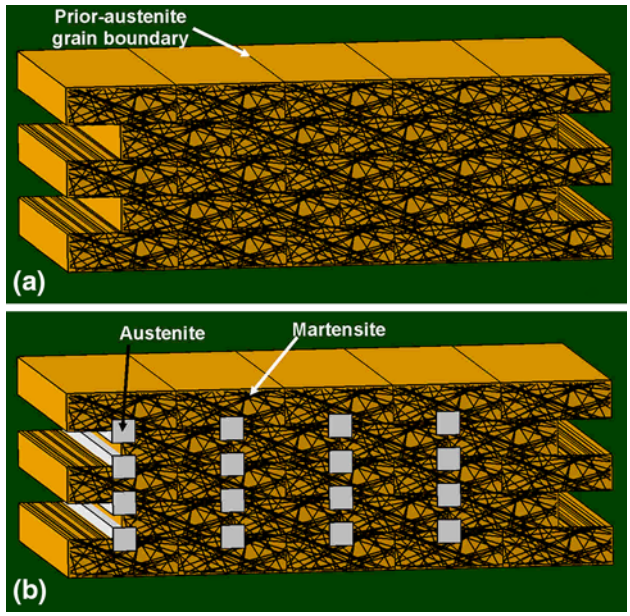

Fig. 14 A schematic of austenite formation at the prior-austenite grain-boundary junctions within a fully martensitic as-hot-rolled microstructure during super-Ac_1 thermal exposure: (a) pre-transformation microstructure; and (b) post-transformation microstructure

Cooling Portion of the Thermal History. In the case of maximum-exposure temperature being over that Ac_1, martensite tempering simply continues (at the progressively lower rate) during cooling to room temperature. Thus, the progress of the martensite-tempering phase transformation can be treated using the methods developed in the previous section. As far as the case of a super-Ac_1 maximum-exposure temperature is concerned, austenite formed undergoes decomposition during subsequent cooling to room temperature. To a first order of approximation, austenite-decomposition phase transformations can be handled using the same approach as the one developed in the context of FZ. One of the significant differences to be accounted for is the fact that austenite, in the present case if formed within the Ac_1-Ac_3 temperature range possesses a different chemical composition than its counterpart in the FZ. Specifically, due to the hypoeutectoid character of MIL A46100, austenite formed in this temperature range is enriched on alloying elements relative to the nominal chemical composition of MIL A46100. Consequently, and supported by the

results displayed in Fig. 7(a) to (e), austenite is less likely to transform into one of its high-temperature decomposition products, i.e., allotriomorphic ferrite and/or Widmanstatten ferrite. Additional potential difference between the austenite decomposition reactions in HAZ from that in FZ is related to the fact that austenite/ferrite interfaces may already exist at the onset of cooling, hence, ferrite nucleation is not required and the overall progress of austenite to ferrite transformation is controlled by the growth, rather than nucleation, kinetics.

2.5 Microstructure/Property Relationship Module

In this module, functional relationships between the material microstructure (quantified primarily by the corresponding volume fractions) and the material properties (primarily mechanical properties such as hardness, toughness, etc.) are used to determine spatial distribution of the material properties throughout different weld regions. The establishment of these functional relationships has been one of the main goals of the field of physical metallurgy for over half a century and remains a challenge. Nevertheless, for MIL A46100, various experimental methods have been employed to help establish functional relationships between the volume fractions of martensite, bainite, ferrite, pearlite, and retained austenite, prior austenite grain size, and the material hardness (Ref 53). These functional relationships are adopted in this study. They suggest that, to a first order of approximation, material strength/hardness is related to the volume fractions and hardnesses of the aforementioned phases and microstructural constituents via the simple rule-of-mixture type functions (Ref 54, 55), while the effect of the prior austenite grain size is consistent with the so-called Hall-Petch relation (Ref 56–58). The microstructure evolution module yields the prediction of the local phase/microconstituent volume fractions, while the phase/microconstituent hardnesses have to be determined experimentally using techniques such as micro/nanoindentation. Due to space limitations, details regarding the functional relationships between the material strength/hardnesses and the aforementioned aspects of the material microstructure and the constituent hardnesses will be presented in our future communication.

3. Results and Discussion

The multiphysics GMAW process model described in the previous section is applied to MIL A46100 in order to demonstrate the ability of the model to establish correlations between the welding-process parameters and the resulting as-welded material microstructure and properties (as well as their spatial distributions throughout the weld region). Due to space constraints, only a few typical results will be presented and discussed in the remainder of this section. Some of these results are shown in order to merely showcase the overall potential of the present approach, but not discussed in great detail. For example, the results pertaining to the spatial distribution of the equivalent plastic strain and the residual von Mises stress in the weldment could be potentially quite important relative to the overall functional and mechanical performance of the GMAW joint. On the other hand, detailed results pertaining to the spatial distribution and temporal evolution of the temperature within the FZ and the HAZ (and their dependence on the GMAW process parameters) are the key input to the computational analysis dealing with the prediction of the material microstructure and property distributions within the weld region.

3.1 Typical Results

3.1.1 Temporal Evolution of the Weldment Temperature Field. Figure 15(a) to (d) shows typical results pertaining to the temporal evolution of the temperature field within the weld region over the (analyzed) right-portion of the weldment. The results displayed in Fig. 15(a) to (d) are obtained at relative welding times of 0.6, 2.1, 3.6, and 4.8 s, respectively, and for the following selection of the GMAW process parameters: welding open-circuit voltage = 30 V, welding current = 200 A, electrode diameter = 1 mm, electrode-tip/weld distance = 1.3 cm, electrode feed-rate = 10 cm/s, and gun travel speed = 1 cm/s. To improve clarity, regions of the weldment with a temperature exceeding the liquidus temperature are denoted using red.

Examination of the results displayed in Fig. 15(a) to (d) reveals that: (a) the FZ, after a brief transient period, acquires a nearly constant size and shape, as it moves along the welding direction (to track the position of the weld gun); (b) as welding proceeds, natural convection, and radiation to the surroundings, together with conduction through the adjacent work-piece material region, cause the previously molten material within the FZ to solidify (and to continue to cool); and (c) under the given welding conditions, the FZ extends downward by approximately 40-45% of the workpiece thickness.

The effect of GMAW process parameters on the temperature distribution is exemplified by the results depicted in Fig. 16(a) and (b). The results displayed in these figures were obtained under identical GMAW process conditions except for the value of the open-circuit voltage, set equal to 30 V and 35 V for the cases displayed in Fig. 16(a) and (b), respectively. As expected, it is seen that an increase in the welding voltage/power increases the size of the FZ.

3.1.2 Temporal Evolution of Temperature at Specific Locations Within the FZ and HAZ. Typical results pertaining to the temporal evolution of temperature at fixed locations within the FZ and HAZ are shown in Fig. 17(a) and (b), respectively. The results displayed in Fig. 17(a) pertain to the weldment (through-the-thickness) mid-plane within the FZ. Curve labels are used to denote the distance of the material point in question from the weld y-z symmetry plane. The results displayed in Fig. 17(b), on the other hand, also pertain to the weldment mid-plane, but within the HAZ, while the curve labels used in this case represent the distance of the material point in question from the FZ/HAZ interface. It should be noted that the phase volume fractions in the FZ and HAZ are computed in the next section from similar results but for a larger number of closely spaced material points.

Examination of the results displayed in Fig. 17(a) and (b) reveals that: (a) material points which reside within the FZ experience temperatures in excess of the MIL A46100 liquidus temperature (1772 K). These points are subjected to a steep rise in temperature, as a result of the arrival of the weld gun, and a relatively steep drop in temperature, as a result of the departure of the weld gun; (b) material points which reside within the HAZ experience temperatures which are in excess of the MIL A46100 Ac_1 temperature (982 K) but which are lower than the MIL A46100 liquidus temperature. These points are subjected

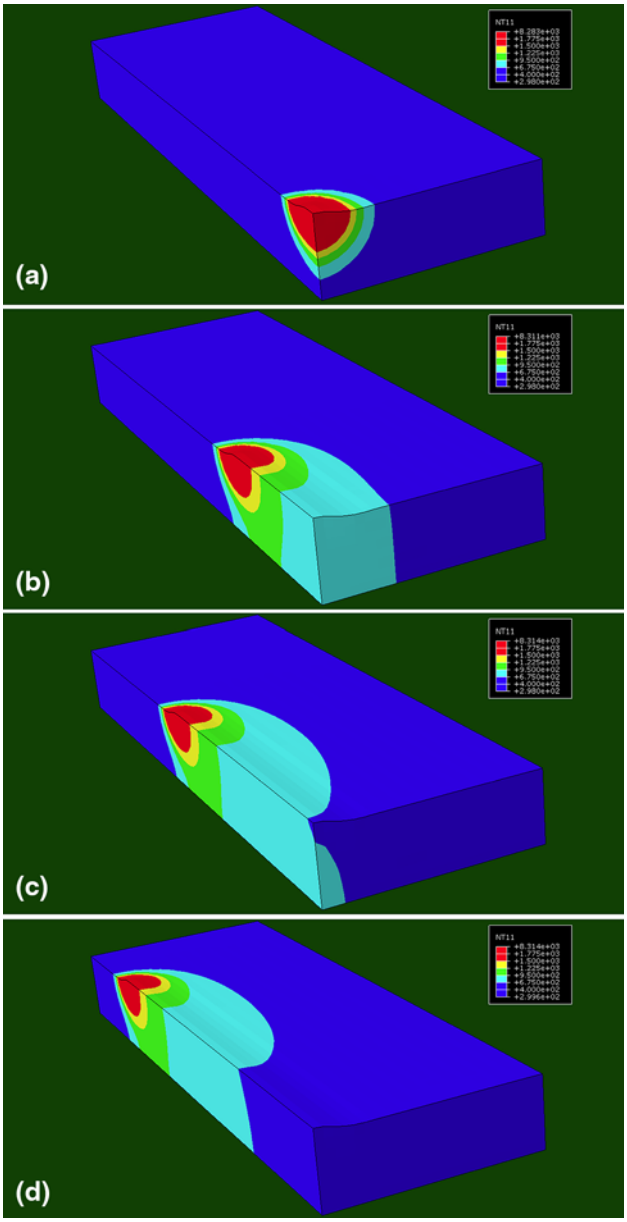

Fig. 15 Typical results pertaining to the spatial distribution of the temperature field in the weld region over the (analyzed) right-portion of the MIL A46100 weldment at welding times of: (a) 0.6 s; (b) 2.1 s, (c) 3.6 s; and (d) 4.8 s under the following welding conditions: welding open-circuit voltage = 30 V, welding current = 200 A, electrode diameter = 1 mm, electrode-tip/weld distance = 1.3 cm, electrode feed-rate = 10 cm/s, and gun travel speed = 1 cm/s

to a significantly lower heating rate, spend more time at temperatures near the peak temperature and undergo relatively slow cooling; and (c) as expected, the maximum temperature experienced by the material points, both within the FZ and HAZ, decreases with an increase in distance from the weld centerline.

3.1.3 Thermal-Strain/Residual-Stress Fields. Non-uniformity in the temperature distribution throughout the weld region, if sufficiently large, may give rise to high thermal stresses and, in turn, plastic deformation (permanent distortion). This may particularly take place within the FZ due to highly

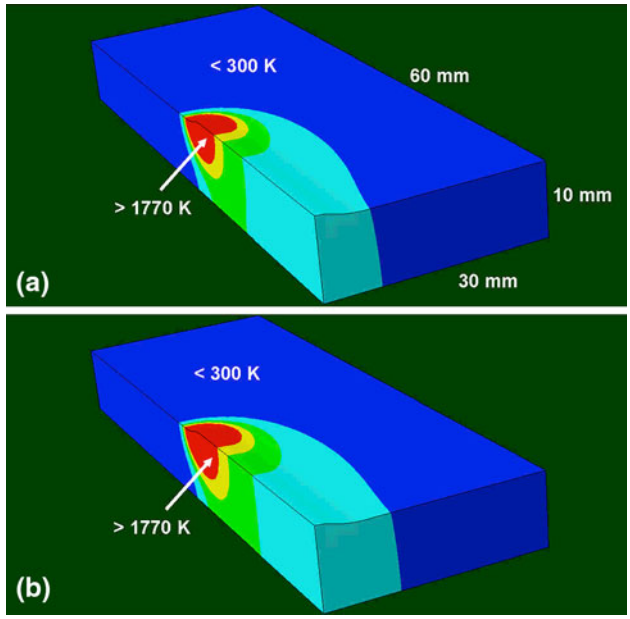

Fig. 16 Typical results showing the effect of welding open-circuit voltage, 30 V in (a) and 35 V in (b) on the spatial distribution of temperature under the identical remaining welding parameters (including the distance traveled by the welding-gun). The remaining parameters are: welding current = 200 A, electrode diameter = 1 mm, electrode-tip/weld distance = 1.3 cm, electrode feed-rate = 10 cm/s, and gun travel speed = 1 cm/s

non-uniform input thermal flux, as seen in Fig. 3. Should plastic deformation occur, weldments will acquire residual stresses upon cooling to room temperature. As explained earlier, due to its thermomechanical character, the present multiphysics GMAW process model is capable of predicting the development of such welding-induced permanent distortions and residual stresses. Examples of the thermal-strain/residual-stress results obtained using the present GMAW process model are shown in Fig. 18(a) and (b). Figure 18(a) and (b) shows, respectively, spatial distribution of the equivalent plastic strain and the von Mises equivalent residual stress over a transverse section of the weld. For improved clarity, contour-level legends are not displayed. Rather, the maximum values of the equivalent plastic strain and the von Mises equivalent residual stress are denoted in these figures. Examination of the results displayed in Fig. 18(a) and (b) shows that, as anticipated, the largest plasticity/residual-stress effects are observed within the FZ as well as the adjacent portions of the HAZ.

Welding-induced permanent distortions may, due to the resulting shape and dimensional changes, affect functional performance of a weldment while the presence of the (tensile) residual stresses may degrade structural performance and/or affect reliability/durability of the weld. It should also be noted that the plastic strains and residual stresses may also affect the progress of the austenite $\rightarrow$ bainite and austenite $\rightarrow$ martensite displacive phase transformations, via the so-called "*deformation-induced*" and "*stress-assisted*" transformation effects (Ref 56). While these effects may somewhat affect the predictions of the microstructure distribution within the weld (presented in the next section), they will not be discussed in greater detail here. Our preliminary investigation suggested that, within the common GMAW process parameter envelope, the role of these effects is relatively small.

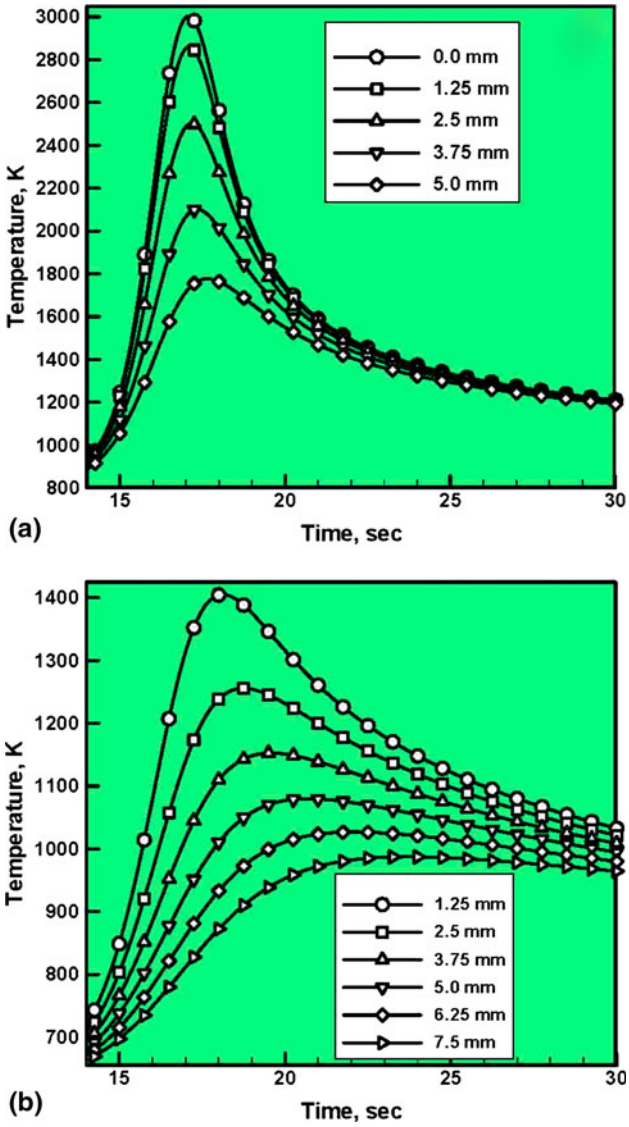

Fig. 17 Typical results pertaining to the temporal evolution of temperature: (a) along the workpiece mid-plane within the FZ (the curve labels denote the distance of the subject material point from the weld *y-z* symmetry plane); and (b) along the workpiece mid-plane within the HAZ (the curve labels denote the distance of the subject material point from the HAZ/FZ interface)

3.2 Room-Temperature Weld Microstructure Prediction

In this section, the thermal history results like the ones reported in Fig. 17(a) and (b) are used as input to the FZ and HAZ microstructure-evolution analyses presented in section 2 in order to determine the room-temperature volume fractions of all the crystalline phases and microconstituents within the weld region. It should be recalled that the analyses presented in the microstructure evolution module, section 2.4, revealed that the nature of the phase transformations encountered and their thermodynamic/kinetic relations are drastically different for the material points residing within the FZ and the HAZ. As a result, different microstructural-evolution functional relationships were applied, in this portion of the work, to the material points residing in these two portions of the weld region. The results pertaining to the spatial variation of the phase volume fractions within the FZ and the HAZ are ultimately combined to

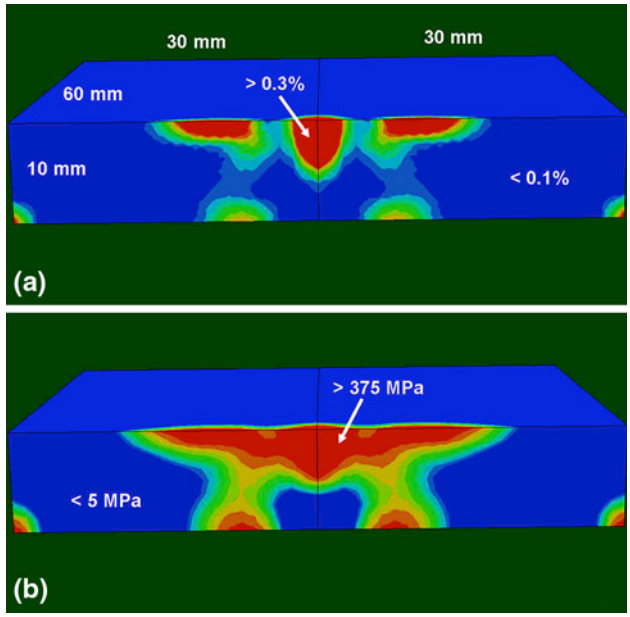

Fig. 18 Typical results pertaining to the spatial distribution of: (a) equivalent plastic strain; and (b) residual von Mises equivalent stress over a transverse section of the weld and the workpiece region adjacent to the weld

construct the corresponding contour plots for the entire weld region. It should be also noted that all the analyses carried out in this portion of the study pertain to the case of MIL A46100, initially in the as-hot-rolled and self-tempered martensitic state and the following GMAW process parameters: welding open-circuit voltage = 30 V, welding current = 200 A, electrode diameter = 1 mm, electrode-tip/weld distance = 1.3 cm, electrode feed-rate = 10 cm/s, and gun travel speed = 1 cm/s. Under these conditions, and in accordance with the detailed analysis of phase transformations within MIL A46100, and considering details of the microstructure-evolution analyses presented in section 2.4, any material point within the weld region may contain up to five of the following microconstituents: (a) allotriomorphic ferrite; (b) Widmanstatten ferrite; (c) bainite; (d) freshly formed martensite; and (e) tempered martensite.

The results obtained in this portion of this study under the aforementioned conditions are depicted in Fig. 19(a) to (f). In Fig. 19(a) to (e), the spatial distributions of phase volume fractions over a transverse section of the weld and the workpiece region adjacent to the weld are presented for: (a) allotriomorphic ferrite; (b) Widmanstatten ferrite; (c) bainite; (d) freshly formed martensite; and (e) tempered martensite, respectively. In Fig. 19(f), the corresponding spatial distribution of the prior-austenite grain size is shown. Examination of the results displayed in Fig. 19(a) to (f) reveals that:

(a) As seen in Fig. 19(a) and (b), allotriomorphic ferrite and Widmanstatten ferrite are both present only within the FZ, and this observation is fully consistent with the fact that the material within this region is initially subjected to temperatures substantially higher than the material liquidus temperature and, consequently, undergoes relatively slow cooling. In addition, the material within the FZ possesses relatively low hardenability, since austenite chemical composition is nearly identical to that of the alloy itself;

(b) As seen in Fig. 19(d), the volume fraction of freshly formed martensite within the FZ is fairly small (less than 30 vol.%). This finding is consistent with the relatively low cooling rates and with the relatively low hardenability of austenite found in this weld region. As one crosses the FZ/HAZ interface and enters the HAZ, the volume fraction of freshly formed martensite first increases (to a value in excess of 85 vol.%) and then decreases (to a value of ca. 10 vol.%). The volume fraction of the freshly formed martensite drops to zero once the HAZ/unaffected-material boundary is crossed. This spatial distribution of the volume fraction of freshly formed martensite is a consequence of a trade-off between the amount of austenite available to transform into martensite and the hardenability (ease of transformation) of austenite into martensite. Specifically, in the HAZ regions which were exposed to temperatures above Ac_3, full austenitization (100 vol.% austenite) is assumed to take place. However, this austenite possesses low hardenability. On the other hand, as one enters the intercritical region, within which the maximum exposure temperature is between Ac_1 and Ac_3, austenitization becomes incomplete but the attendant austenite possesses higher hardenability. Consequently, as the maximum exposure temperature decreases from Ac_3 to Ac_1, the volume fraction of the freshly formed martensite first increases due to the dominating effect of the increased austenite hardenability. However, after passing through a peak value, the volume fraction of freshly formed martensite decreases, as a result of a lower volume fraction of austenite available for transformation to martensite. Clearly, when the maximum exposure temperature is below Ac_1, no austenitization takes place during heating and, hence, austenite $\rightarrow$ (freshly-formed) martensite phase transformation takes place;

(c) Since the austenite $\rightarrow$ bainite phase transformation is mainly competing with the austenite $\rightarrow$ (freshly formed) martensite phase transformation, variation of the volume fraction of bainite throughout the FZ and within the HAZ (as a function of distance from the FZ/HAZ interface), Fig. 19(c), is a mere reflection of the outcome of this competition;

(d) As seen in Fig. 19(e), tempered martensite is not present in the FZ, or within the portion of the HAZ which was fully austenitized. In the remainder of the HAZ, volume fraction of tempered martensite increases with distance from the FZ/HAZ interface and ultimately reaches a value of 100%, at a locus of the HAZ points with a maximum exposure temperature of Ac_1; and

(e) As seen in Fig. 19(f), as one moves toward the top-center point of the FZ, the grain size first continuously increases from its initial value (40 microns), to a value of $\sim$ 80 microns near the HAZ/FZ interface. As one enters the FZ, the grain size first drops (the "*chill-zone*" effect) and then continues to increase toward the final value of about 70 microns.

3.3 Room-Temperature Weld-Properties Prediction

In this section, the microstructure/property-relationship module, section 2.5, is used in order to determine spatial distribution of the material hardness within the weld region from the knowledge of the corresponding distributions of the crystalline phase/microconstituent volume fractions (as reported in section 3.2) and their corresponding hardnesses. The results presented in this section all pertain to MIL A46100, initially in the as-hot-rolled and self-tempered martensitic state, and to the following GMAW process parameters: open-circuit voltage = 30 V, welding current = 200 A, electrode diameter = 1 mm, electrode-tip/weld distance = 1.3 cm, electrode feed-rate = 10 cm/s, and gun travel speed = 1 cm/s. As mentioned earlier, the present multiphysics GMAW process model enables prediction of the spatial distribution of material mechanical properties (e.g., hardness) throughout the weld, under any set of process parameters. However, due to space limitations, a detail analysis of the effect of the GMAW process parameters on the material hardness distribution throughout the weld region is deferred to one of our future communications.

As mentioned in section 2.5, the effective hardness of a material point within the weld region is assumed to be given by the simple rule of mixtures applied to the constituent phases' hardnesses. In addition, the effect of the prior-austenite grain size is assumed to be governed by the Hall-Petch relation. By reviewing open-literature data for steel crystalline-phase/microconstituent hardnesses (and their compositional dependence) (Ref 53-55), the following hardness values are adopted: (a) allotriomorphic ferrite—DPH 200; (b) Widmanstatten ferrite—DPH 280; (c) bainite—DPH 400; (d) freshly formed martensite—DPH 600; and (e) tempered martensite—DPH 450.

Using the spatial-distribution microstructure data displayed in Fig. 19(a) to (f) and these crystalline-phase hardnesses, the corresponding spatial distribution of the MIL A46100 hardness (in MPa) within the weld region is computed and depicted in Fig. 20. Examination of the results displayed in this figure revealed that: (a) the material within the FZ which possesses the as-cast microstructure dominated by allotriomorphic and Widmanstatten ferrite has a hardness which is lower than that in the as-received condition of the material; (b) there is a region (i.e., the previously mentioned "*intercritical region*") within which the material possesses a hardness substantially higher than the one in the as-received material; and (c) both the low-hardness and the high-hardness regions are of concern since the low-hardness region compromises the load-bearing capacity of the weldment while the high-hardness region, through the accompanying loss of toughness/ductility, may compromise weldment reliability/durability.

3.4 Model Validation

The analysis of the results pertaining to the spatial distribution of the material microstructure and properties within the MIL A46100 weld region, presented in the previous section, confirmed that the predictions made by the present GMAW process model are in good qualitative agreement with general expectations and prior observations. Unfortunately, quantitative validation of the present model cannot be carried out for a number of reasons: (a) No welding facilities were available to allow an experimental validation of the results obtained in this study. However, GMAW experimental facilities are currently being developed/assembled in order to support the ongoing GMAW modeling and simulation efforts. Once these facilities have been completed, they will enable a full quantitative validation of the present multiphysics GMAW

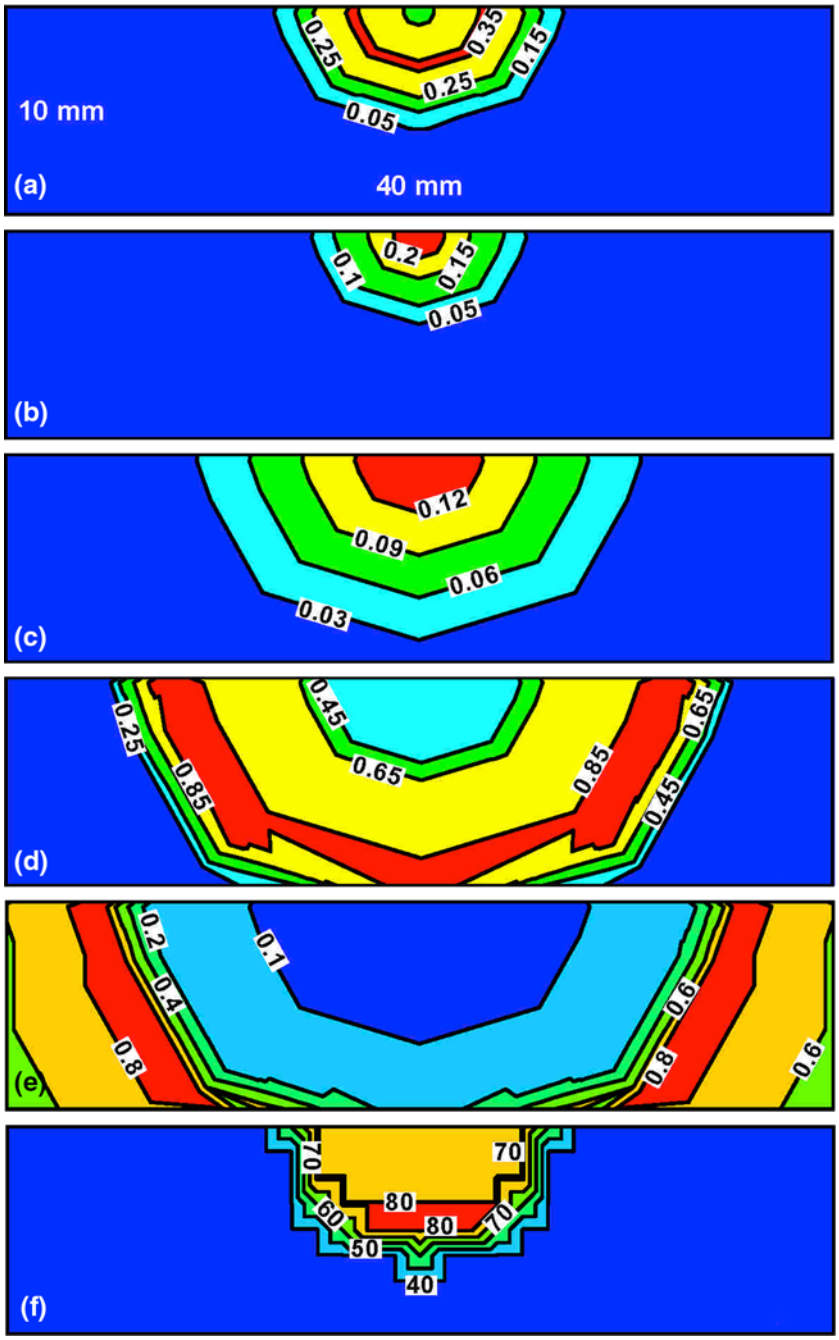

Fig. 19 Typical results pertaining to the spatial distribution of phase volume fractions for: (a) allotriomorphic ferrite; (b) Widmanstatten ferrite; (c) bainite; (d) freshly formed martensite; (e) tempered martensite; and (f) grain size (in microns) over a transverse section of the weld and the workpiece region adjacent to the weld

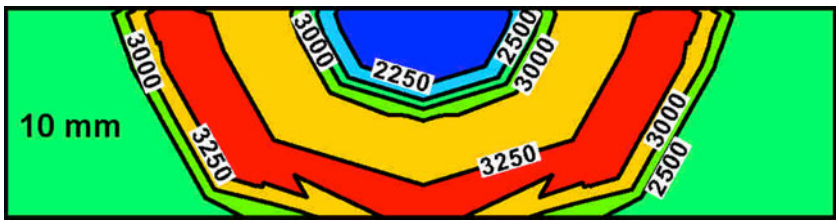

Fig. 20 Typical spatial distribution of the material hardness (in MPa) within the weld region of MIL A46100

process model; and (b) No open-literature experimental results pertaining to the spatial distribution of various crystalline phases and microstructures within the weld region, for the case of MIL A46100 workpiece material and MIL A46100 filler material, could be found. In Ref 30, weld microstructure results are presented for the case of MIL A46100 workpiece material and AWS E11018M filler material. Chemical analysis results obtained in Ref 30 revealed that, due to differences in the chemical compositions of the workpiece and filler materials, significant solid-state diffusion takes place within the HAZ near the FZ/HAZ interface. These diffusion effects alter locally the workpiece material chemical composition and, hence, relative stability of different crystalline phases (as quantified by the corresponding quasi-binary phase, TTT, and CCT diagrams). Consequently, the microstructure distribution results within the FZ and the HAZ portions affected by solid-state diffusion reported in Ref 30 could not be directly compared with the present computational results. However, such a comparison had been made for the HAZ region, which is further away from the FZ/HAZ interface. This comparison revealed that the two sets of results are mutually consistent.

4. Summary and Conclusions

Based on the study presented in this article, the following main summary remarks and conclusions can be made:

1. A new multiphysics computational model for the conventional GMAW joining process has been developed. The model is subsequently applied to analyze butt-welding of MIL A46100, a prototypical high-hardness armor martensitic steel.
2. For convenience, the model has been divided into five interacting modules, each responsible for one of the following five aspects of the GMAW process: (a) dynamics of welding-gun behavior; (b) heat transfer from the electric arc and mass transfer from the electrode to the weld; (c) development of thermal and mechanical fields during the GMAW process; (d) the associated evolution and spatial distribution of the material microstructure throughout the weld region; and (e) the final spatial distribution of the as-welded material properties.
3. The multiphysics GMAW process model developed enables establishment of the functional relationships between the process parameters, e.g., open-circuit voltage, welding current, electrode-to-workpiece distance, filler-metal feed rate, welding-gun speed, etc., and the resulting spatial distribution of the material microstructure (as represented by the volume fractions of various crystallographic phases and microconstituents as well as by the prior-austenite grain size) and properties (primarily hardness) within the weld region.
4. Application of the GMAW process model to the subject material, MIL A46100, yielded the results pertaining to the spatial distribution of the volume fractions of various crystalline phases and microconstituents (within the MIL A46100 GMAW FZ and HAZ) which are qualitatively consistent with their experimental counterparts reported in the open literature.

Acknowledgments

The material presented in this article is based on the work supported by two Army Research Office sponsored grants (W911NF-11-1-0207 and W911NF-09-1-0513) and two U.S. Army/Clemson University Cooperative Agreements (W911NF-04-2-0024 and W911NF-06-2-0042). The authors are indebted to Dr. Larry C. Russell, Jr. of ARO for his continuing support and interest in this study.

References

1. M.G.H. Wells, R.K. Weiss, and J.S. Montgomery, *LAV Armor Plate Study*, MTL TR 92-26, U.S. Army Materials Technology Laboratory, Watertown, MA, 1992
2. J.G. Holmes and B.J. Resnick, Flexible Robot Arc Welding System, *Soc. Manuf. Eng.*, 1979, MS (79)
3. U.S. Environmental Protection Agency, *AP 42, Fifth Edition: Compilation of Air Pollutant Emission Factors, Volume 1: Stationary Point and Area Sources*, U.S. Environmental Protection Agency, Washington, 1995, p 12.19-1–12.19-3
4. A.D. Althouse, C.H. Turnquist, W.A. Bowditch, K.E. Bowditch, and M.A. Bowditch, *Modern Welding*, 10th ed., Goodheart-Willcox Publisher, Tinley Park, IL, 2004, p 233–265
5. M. Grujicic, S. Ramaswami, J.S. Snipes, R. Yavari, A. Arakere, C-F. Yen, and B.A. Cheeseman, Computational Modeling of Microstructure Evolution in AISI 1005 Steel During Gas Metal Arc Butt Welding, *J. Mater. Eng. Perform.*, 2012. doi:10.1007/s11665-012-0402-1
6. M. Grujicic, A. Arakere, S. Ramaswami, J.S. Snipes, R. Yavari, C-F. Yen, B.A. Cheeseman and J.S. Montgomery, Gas Metal Arc Welding Process Modeling and Prediction of Weld Microstructure in MIL A46100 Armor-Grade Martensitic Steel, *J. Mater. Eng. Perform.*, 2013, **22**, p 1541–1557. doi:10.1007/s11665-012-0445-3
7. W. Zhang, J.W. Elmer, and T. DebRoy, Modeling and Real Time Mapping of Phases During GTA Welding of 1005 Steel, *Mater. Sci. Eng. A*, 2002, **333**, p 320–335
8. Ø. Grong, *Metallurgical Modelling of Welding*, 2nd ed., The Institute of Materials, London, 1997
9. K. Easterling, *Introduction to the Physical Metallurgy of Welding*, 2nd ed., Butterworth Heinemann, Boston, 1992
10. L.-E. Svensson, *Control of Microstructures and Properties in Steel Arc Welds*, CRC Press, Boca Raton, 1994
11. R. Mancini and C. Budde, Reaustenitisation in Fe-C Steels Revisited, *Acta Mater.*, 1999, **47**, p 2907–2911
12. R.C. Reed, T. Akbay, Z. Shen, J.M. Robinson, and J.H. Root, Determination of Reaustenitisation Kinetics in a Fe-0.4C Steel Using Dilatometry and Neutron Diffraction, *Mater. Sci. Eng. A*, 1998, **256**, p 152–165
13. J.H. Valentich, *Tube Type Dilatometers: Applications from Cryogenic to Elevated Temperatures*, Instrument Society of America, Research Triangle Park, NC, 1981
14. K.L. Moore, D.S. Naidu, R. Yender, and J. Tyler, Gas Metal Arc Welding Control: Part I—Modeling and Analysis, *Nonlinear Anal. Theory, Methods Appl.*, 1997, **30**, p 3101–3111
15. J. Haidar, A Theoretical Model for Gas Metal Arc Welding and Gas Tungsten Arc Welding. I, *J. Appl. Phys.*, 1998, **84**, p 3518–3529
16. J. Haidar, Prediction of Metal Droplet Formation in Gas Metal Arc Welding. II, *J. Appl. Phys.*, 1998, **84**, p 3530–3540
17. J. Haidar, An Analysis of Heat Transfer and Fume Production in Gas Metal Arc Welding. III, *J. Appl. Phys.*, 1998, **85**, p 3448–3459
18. Z. Bingul and G.E. Cook, Dynamic Modeling of GMAW Process, *Proceedings of the IEEE International Conference on Robotics and Automation*, Detroit, Vol. 4, p 3059–3064
19. Z. Bingul and G.E. Cook, A Real-Time Prediction Model of Electrode Extension for GMAW, *IEEE/ASME Trans. Mechatron.*, 2006, **11**, p 47–54
20. T.P. Quinn, R.B. Madigan, and T.A. Siewert, An Electrode Extension Model for Gas Metal Arc Welding, *Weld. J.*, 1994, **73**, p 241–248

21. J. Goldak, A. Chakravarti, and M. Bibby, A New Finite Element Model for Welding Heat Sources, *Metall. Mater. Trans. B*, 1984, **15**, p 299–305
22. N.T. Nguyen, A. Ohta, K. Matsuoka, N. Suzuki, and Y. Maeda, Analytical Solutions for Transient Temperature of Semi-Infinite Body Subjected to 3-D Moving Heat Sources, *Weld. J.*, 1999, **78**, p 265–274
23. M. Grujicic, R. Galgalikar, J.S. Snipes, R. Yavari, S. Ramaswami, Multi-Physics Modeling of the Fabrication and Dynamic Performance of All-Metal Auxetic-Hexagonal Sandwich-Structures, *Mater. Design*, 2013, **51**, p 113–130. doi:10.1016/j.matdes.2013.04.004
24. S. Ohring and H.J. Lugt, Numerical Simulation of a Time-Dependent 3-D GMA Weld Pool Due to a Moving Arc, *Weld. J.*, 1999, **78**, p 416–424
25. G.M. Oreper, T.W. Eagar, and J. Szekely, Convection in Arc Weld Pools, *Weld. J. Res. Suppl.*, 1983, **62**, p 307–312
26. S.Y. Lee and S.J. Na, Numerical Analysis of Molten Pool Convection Considering Geometric Parameters of Cathode and Anode, *Weld. J.*, 1997, **76**, p 484–497
27. Z. Cao, Z. Yang, and X.L. Chen, Three-Dimensional Simulation of Transient GMA Weld Pool with Free Surface, *Weld. J.*, 2004, **83**, p 169–176
28. J. Hu and H.L. Tsai, Heat and Mass Transfer in Gas Metal Arc Welding. Part I: The Arc, *Int. J. Heat Mass Transf.*, 2007, **50**, p 833–846
29. J. Hu and H.L. Tsai, Heat and Mass Transfer in Gas Metal Arc Welding. Part II: The Metal, *Int. J. Heat Mass Transf.*, 2007, **50**, p 808–820
30. S.J. Unfried, C.M. Garzón, and J.E. Giraldo, Numerical and Experimental Analysis of Microstructure Evolution During Arc Welding in Armor Plate Steels, *J. Mater. Process. Technol.*, 2009, **209**, p 1688–1700
31. Y.-A. Song, S. Park, and S.-W. Chae, 3D Welding and Milling: Part II—Optimization of the 3D Welding Process Using an Experimental Design Approach, *Int. J. Mach. Tools Manuf.*, 2005, **45**, p 1063–1069
32. V. Pavelic, R. Tanbakuchi, O.A. Uyehara, and P.S. Myers, Experimental and Computed Temperature Histories in Gas Tungsten-Arc Welding of Thin Plates, *Weld. J. Res. Suppl.*, 1969, **48**, p 295–305
33. D. Kim, "*Prediction of Microstructure Evolution of Heat-Affected Zone in Gas Metal Arc Welding of Steels*," Ph.D. dissertation, University of Texas, Austin, 2012
34. M. Grujicic, G. Arakere, B. Pandurangan, A. Hariharan, C.-F. Yen, B.A. Cheeseman, and C. Fountzoulas, Computational Analysis and Experimental Validation of the Ti-6Al-4V Friction Stir Welding Behavior, *J. Eng. Manuf.*, 2010, **224**, p 1–16
35. M. Grujicic, T. He, G. Arakere, H.V. Yalavarthy, C.-F. Yen, and B.A. Cheeseman, Fully-Coupled Thermo-Mechanical Finite-Element Investigation of Material Evolution During Friction-Stir Welding of AA5083, *J. Eng. Manuf.*, 2010, **224**, p 609–625
36. M. Grujicic, G. Arakere, H.V. Yalavarthy, T. He, C.-F. Yen, and B.A. Cheeseman, Modeling of AA5083 Material-Microstructure Evolution During Butt Friction-Stir Welding, *J. Mater. Eng. Perform.*, 2010, **19**, p 672–684
37. M. Grujicic, G. Arakere, B. Pandurangan, A. Hariharan, C.-F. Yen, and B.A. Cheeseman, Development of a Robust and Cost-Effective Friction Stir Welding Process for Use in Advanced Military Vehicle Structures, *J. Mater. Eng. Perform.*, 2011, **20**, p 11–23
38. M. Grujicic, G. Arakere, C.-F. Yen, and B.A. Cheeseman, Computational Investigation of Hardness Evolution During Friction-Stir Welding of AA5083 and AA2139 Aluminum Alloys, *J. Mater. Eng. Perform.*, 2011, **20**, p 1097–1108
39. M. Grujicic, G. Arakere, A. Hariharan, and B. Pandurangan, A Concurrent Product-Development Approach for Friction-Stir Welded Vehicle-Underbody Structures, *J. Mater. Eng. Perform.*, 2012, **21**, p 437–449
40. M. Grujicic, G. Arakere, A. Hariharan, and B. Pandurangan, Two-Level Weld-Material Homogenization Approach for Efficient Computational Analysis of Welded Structure Blast Survivability, *J. Mater. Eng. Perform.*, 2012, **21**, p 786–796
41. M. Grujicic, G. Arakere, B. Pandurangan, J.M. Ochterbeck, C.-F. Yen, B.A. Cheeseman, A.P. Reynolds, and M.A. Sutton, Computational Analysis of Material Flow During Friction Stir Welding of AA5059 Aluminum Alloys, *J. Mater. Eng. Perform.*, 2012, **21**, p 1824–1840
42. M. Grujicic, B. Pandurangan, C.-F. Yen, and B.A. Cheeseman, Modifications in the AA5083 Johnson-Cook Material Model for Use in Friction Stir Welding Computational Analyses, *J. Mater. Eng. Perform.*, 2012, **21**, p 2207–2217
43. G.R. Johnson and W.H. Cook, A Constitutive Model and Data for Metals Subjected to Large Strains, High Strain Rates and High Temperatures, *Proceedings of the 7th International Symposium on Ballistics*, The Hague, 1983
44. ABAQUS Version 6.10EF, *User Documentation*, Dassault Systems, 2011
45. MIL STD-A46100 Standard Specification, 1983: Armor Plate Steel Wrought High Hardness
46. J.-O. Andersson, T. Helander, L. Höglund, P. Shi, and B. Sundman, Calphad-Based Thermocalc and Dictra Method, *Calphad*, 2002, **26**, p 273–312
47. H.K.D.H. Bhadeshia, L.-E. Svensson, and B. Gretoft, A Model for the Development of Microstructure in Low-Alloy Steel (Fe-Mn-Si-C) Weld Deposits, *Acta Metall.*, 1985, **33**, p 1271–1283
48. S.J. Jones and H.K.D.H. Bhadeshia, Kinetics of the Simultaneous Decomposition of Austenite into Several Transformation Products, *Acta Mater.*, 1997, **45**, p 2911–2920
49. H. Matsuda and H.K.D.H. Bhadeshia, Kinetics of the Bainite Transformation, *Proc. R. Soc. Lond. A*, 2004, **460**, p 1707–1722
50. P. Kruger, On the Relation Between Non-Isothermal and Isothermal Kolmogorov-Johnson-Mehl-Avrami Crystallization Kinetics, *J. Phys. Chem. Solids*, 1993, **54**, p 1549–1555
51. M. Grujicic and G. Haidemenopoulos, Treatment of Paraequilibrium Thermodynamics in an AF1410 Steel Using the Thermo-Calc Software and Database, *Calphad*, 1988, **12**, p 219–224
52. M. Grujicic, Thermodynamics-Aided Design of High Co-Ni Secondary Hardening Steels, *Calphad*, 1990, **14**, p 49–59
53. G.M. Ludtka, G.M. Ludtka, P. Ray, and J. Magee, "*Magnetic Processing – A Pervasive Energy Efficient Technology for Next Generation Materials for Aerospace and Specialty Steel Markets*," Final CRADA Report for CRADA Number NFE-09-02189, Oak Ridge National Laboratory, 2010
54. J.C. Ion, K.E. Easterling, and M.F. Ashby, A Second Report on Diagrams of Microstructure and Hardness for Heat-Affected Zones in Welds, *Acta Metall.*, 1984, **32**, p 1949–1955
55. P. Maynier, B. Jungmann, and J.D. Creusot-Loire, *System for the Prediction of the Mechanical Properties of Low Alloy Steel Products. Hardenability Concepts with Applications to Steel*, The Metallurgical Society of AIME, Chicago, 1978, p 518–545
56. M. Gore, M. Grujicic, and G.B. Olson, Thermally Activated Grain Boundary Motion Through a Dispersion of Particles, *Acta Metall.*, 1989, **37**, p 2849–2854
57. M. Grujicic, G. Cao and P.F. Joseph, Multi-Scale Modeling of Deformation and Fracture of Polycrystalline Lamellar γ-TiAl + α_2-Ti_3Al Alloys, *Int. J. Multiscale Comput. Eng.*, 2003, **1**, p 1–21
58. R.S. Miller, G. Cao and M. Grujicic, Monte Carlo Simulation of Three-Dimensional Non-Isothermal Grain-Microstructure Evolution: Application to LENS™ Rapid Fabrication, *J. Mater. Synth. Proces.*, 2001, **9**, p 329–345